OULU 2014
D 1265

ACTA UNIVERSITATIS OULUENSIS

Anna-Leena Manninen

CLINICAL APPLICATIONS OF RADIOPHOTOLUMINESCENCE (RPL) DOSIMETRY IN EVALUATION OF PATIENT RADIATION EXPOSURE IN RADIOLOGY

DETERMINATION OF ABSORBED AND EFFECTIVE DOSE

UNIVERSITY OF OULU GRADUATE SCHOOL;
UNIVERSITY OF OULU,
FACULTY OF MEDICINE,
INSTITUTE OF DIAGNOSTICS,
DEPARTMENT OF DIAGNOSTIC RADIOLOGY;
OULU UNIVERSITY HOSPITAL;
MEDICAL RESEARCH CENTER OULU

ACTA UNIVERSITATIS OULUENSIS
D Medica 1265

ANNA-LEENA MANNINEN

CLINICAL APPLICATIONS OF RADIOPHOTOLUMINESCENCE (RPL) DOSIMETRY IN EVALUATION OF PATIENT RADIATION EXPOSURE IN RADIOLOGY

Determination of absorbed and effective dose

Academic Dissertation to be presented with the assent of the Doctoral Training Committee of Health and Biosciences of the University of Oulu for public defence in Auditorium 7 of Oulu University Hospital, on 28 November 2014, at 12 noon

UNIVERSITY OF OULU, OULU 2014

Acta Univ. Oul. D 1265, 2014

Supervised by
Professor Miika Nieminen
Docent Antero Koivula
Doctor Timo Mäkelä

Reviewed by
Docent Mika Kortesniemi
Docent Jari Heikkinen

Opponent
Professor Sauli Savolainen

ISBN 978-952-62-0623-3 (Paperback)
ISBN 978-952-62-0624-0 (PDF)

ISSN 0355-3221 (Printed)
ISSN 1796-2234 (Online)

Cover Design
Raimo Ahonen

JUVENES PRINT
TAMPERE 2014

Manninen, Anna-Leena, Clinical applications of radiophotoluminescence (RPL) dosimetry in evaluation of patient radiation exposure in radiology. Determination of absorbed and effective dose

University of Oulu Graduate School; University of Oulu, Faculty of Medicine, Institute of Diagnostics, Department of Diagnostic Radiology; Oulu University Hospital; Medical Research Center Oulu

Acta Univ. Oul. D 1265, 2014

University of Oulu, P.O. Box 8000, FI-90014 University of Oulu, Finland

Abstract

Computed tomography (CT) and interventional procedures cause relatively high patient doses compared with other imaging modalities in radiology. The optimization of the imaging equipment and procedures is important and necessary due to the known risks caused by ionization radiation. The different irradiation geometries and dose units between imaging techniques complicate the comparison of patients' radiation exposure. Absorbed doses (D) of organs predict the tissue reactions of the procedures, while effective dose (E) is a useful means of comparing the stochastic effects of the different imaging procedures. A and E can be estimated from dosimetric measurements in a phantom. In vivo measurements are used during a radiological examination.

In the present thesis, various properties of radiophotoluminescence dosimeters (RPLD) were investigated to verify the applicability of RPL dosimetry in radiology. The absorbed dose was determined *in vaginal fornix* of seven pregnant women, in the area near the head of the fetus during prophylactic catheterization before uterine artery embolization (UAE). The evaluation of the radiation exposure of digital subtraction angiography (DSA) and computed tomography angiography (CTA) was performed using an anthropomorphic phantom. Absorbed doses of organs and effective dose were determined for a typical four-vessel angiography of the cerebral area, including intracranial vessels, and for the cervicocerebral area, including both cervical and intracranial vessels.

RPLD shows excellent dose linearity and minimal fading. The low dose detection threshold was determined to be 20 µGy with a coefficient of variation (CV) of 12.2%. The methodology is independent of photon energy in the energy range used in radiology. For seven patients studied, the mean value of D *in vaginal fornix* was 11.2 mGy (range 2.2–28.7) being low dose study when pulsed fluoroscopy with an optimized protocol is used without angiography exposures. In the assessment of cerebral vessels, the effective dose for CTA was approximately one-fifth of the dose compared with DSA. The dose for cervicocerebral vessels CTA was approximately one third higher compared with DSA. Conversion factors from the DAP and the DLP to the effective dose were calculated for the specific angiographic protocols. RPL dosimetry shows sufficient reliability in measuring radiation doses in radiology.

Keywords: absorbed dose, CTA, dosimetry, DSA, effective dose, fetus, prophylactic catheterization, radiation exposure, radiology, radiophotoluminescence, UAE

Manninen, Anna-Leena, Radiofotoluminesenssi (RPL) dosimetrian kliiniset sovellukset potilaan säteilyaltistuksen arvioinnissa radiologisissa tutkimuksissa. Absorboituneen ja efektiivisen annoksen määrittäminen

Oulun yliopiston tutkijakoulu; Oulun yliopisto, Lääketieteellinen tiedekunta, Diagnostiikan laitos, Radiologia; Oulun yliopistollinen sairaala; Medical Research Center Oulu

Acta Univ. Oul. D 1265, 2014
Oulun yliopisto, PL 8000, 90014 Oulun yliopisto

Tiivistelmä

Tietokonetomografiakuvauksissa ja toimenpideradiologisissa tutkimuksissa potilaan säteilyaltistus on suhteellisesti korkeampi verrattuna muihin radiologisiin kuvausmenetelmiin. Kuvauslaitteiden erilaiset kuvausgeometriat ja annosyksiköt hankaloittavat potilaan säteilyaltistuksen vertailua eri tutkimusmenetelmien välillä. Kudokseen absorboituneen annoksen (D) avulla arvioidaan ionisoivan säteilyn suoraa haittavaikutusta kudokselle, kun taas efektiivisen annoksen (E) määrittämisellä arvioidaan säteilyn satunnaista haittaa. D ja E voidaan mitata annosmittarilla käyttäen potilasvastinetta. *In vivo* mittauksella saadaan annostietoa tutkimuksen aikana suoraan potilaasta.

Radiofotoluminesenssiannosmittarin (RPLD) soveltuvuus radiologisiin annosmittauksiin varmistettiin tutkimalla mittarin eri fysikaalisia ominaisuuksia. RPLD:a käytettiin intravaginaalisen annoksen mittauksessa seitsemällä raskaana olevalla naisella. Potilaille tehtiin massiivisen verenvuodon ehkäisemiseksi kohdun valtimosuonten katetrointi läpivalaisuohjattuna ennen kohtuvaltimoiden tukkimishoitoa (UAE). Mittaustulokset antavat tietoa kudokseen absorboituneesta annoksesta lähellä syntymätöntä lasta. Tietokonetomografia-angiografia (TTA) ja digitaalinen subtraktioangiografia (DSA) tutkimusten annosmittaukset tehtiin potilasvastineessa käyttäen RPLD:a. Elinannoksista laskettiin efektiivinen annos aivovaltimoiden ja aivokaulavaltimoiden angiografiatutkimuksille.

RPL -annosmittausmenetelmän havaittiin olevan lineaarinen ja annoksen häviäminen mittarista on vähäistä. Matalan annoksen mittausraja oli 20 µGy 12.2% toistettavuudella. RPLD on riippumaton säteilyenergiasta radiologiassa käytettävällä energia-alueella. Seitsemän potilaan keskimääräinen absorboitunut annos oli 11.2 mGy (vaihteluväli 2.2–28.7 mGy) emättimen pohjukasta mitattuna. Annostaso osoittaa, että katetrointitoimenpide on matala-annostutkimus, kun toimenpide tehdään läpivalaisuohjauksessa, eikä angiografisia kuvia käytetä. Aivovaltimoiden TTA:n efektiivinen annos oli viidesosa DSA menetelmän annoksesta. Aivokaulavaltimoiden TTA:n efektiivinen annos oli arviolta 35% korkeampi kuin DSA menetelmän annos. Konversiokertoimet DAP ja DLP yksiköistä efektiivisen annoksen laskemiseksi määritettiin tutkimuksessa käytetyille kuvausohjelmille. RPL -menetelmä osoitti riittävää luotettavuutta radiologisten säteilyannosten mittauksessa.

Asiasanat: absorboitunut annos, CTA, dosimetria, DSA, efektiivinen annos, ennaltaehkäisevä katetrointi, radiofotoluminesenssi, radiologia, sikiö, säteilyaltistus, UAE

Joy in looking and comprehending is nature's most beautiful gift.
–Albert Einstein

To my family

Acknowledgements

This study was carried out at the Department of Diagnostic Radiology, in Oulu University Hospital and the University of Oulu, during the years of 2008–2014.

I owe my greatest gratitude to my primary supervisor, Ph.D., Professor Miika Nieminen, Chief Physicist at the Department of Diagnostic Radiology at Oulu University Hospital, who gave me the impetus for this work and has been an essential advisor, and furthermore, provided the opportunity and facilities for my research. I wish to thank his constructive criticism and advice. Furthermore, his patient attitude and expertise in academic writing was an essential contribution in the finalization of this thesis.

I wish to thank my second supervisor, Ph.D., Docent Antero Koivula for leading me to the world of dosimetry. His expertise in the field of radiation dosimetry, his optimistic attitude and great faith towards my work were substantial to this thesis. I wish to thank my third supervisor, Ph.D., D.Sc. (Tech.), Timo Mäkelä, Hospital Physicist at Department of Cardiology, Oulu University Hospital, for giving me helpful advice and support during the writing process.

I wish to express my sincere gratitude to M.D., Ph.D., Professor Osmo Tervonen, Head of the Institute of Diagnostics, for his encouraging comments and for giving me the opportunity and facilities for this thesis.

I am sincerely thankful to Ph.D., Docent Mika Kortesniemi, Chief Physicist at Helsinki University Hospital, and Ph.D., Docent Jari Heikkinen, Chief Physicist at Etelä-Savo Hospital District, the official reviewers of the thesis, for their constructive comments and suggestions to the manuscript.

I am deeply grateful to my collaborators. I have had the great honor of working with a group of specialists in the field of radiology. Clinical knowledge of the specific examinations was the foundation of this thesis. I would especially like to thank my radiological co-authors: M.D. Ph.D., Ari Karttunen, Head of the Department of Diagnostic Radiology, who gave his personal support as well as the opportunity and facilities for my research, M.D., Ph.D., Topi Siniluoto, whose expertise in neuroradiology, enthusiastic attitude, ideas and curiosity were a significant impetus for the subject under investigation, M.D., Ph.D., Juha-Matti Isokangas, whose patient contribution to completing the laborious phantom simulations, practical advice for writing papers, and expertise in neuroradiology were extremely important, M.D., Ph.D., Jukka Perälä, whose accomplished contribution in the field of interventional radiology was significant, and this study would not have been possible without his support in this thesis. I am also grateful

to M.D., Ph.D., Kati Ojala, whose expertise in the field of obstetrics and gynecology was essential for this thesis. I wish to thank M.D., Ph.D., Juho Kariniemi and M.D., Ph.D., Kari Palosaari for their positive attitude to my research during the demanding interventional treatments.

I owe my warm thanks to the staff of Diagnostic Radiology, who have always been patient and helpful with my research. They were kind and understanding in helping me train for the use of the imaging equipment and the arrangement of study schedules in addition to busy patient work.

I want to express my warmest thanks to my colleagues for interesting discussions in the field of radiology, which were helpful in understanding medical physics. Especially, I want to thank M.Sc. (Tech.), Hospital Physicist, Pentti Torniainen for his expertise in the field of medical imaging in helping me to solve the practical problems with the imaging protocols.

I am grateful to M.A., Anna Vuolteenaho for her work in revising the language of this thesis.

I wish to thank my friends for their patience in waiting for the day when I have time to get on with leisure activities.

I wish to express my warmest thanks to my parents, Elna and Niilo for support and being models of persistence. I am grateful to my brothers and sisters and to their families; I have always been able to trust them. Especially Jouko, you have always been at my disposal and helpful when I have needed help with problems in the English language.

My deepest gratitude and loving thoughts go to my family, my husband Juha and our children, Joonas, Joel and Enni, who believed in me during this long project and believed that it would be finished someday, and that mother's thoughts would be more in the present than they had been for years. My dear children, you have grown up to be young adults and fine persons during my studying years. Juha, without you assuming responsibility for the weekly routine with our children, this project would not have been possible. Your great sense of humor in the daily routines and encouraging support towards my work has carried me through this project.

Oulu, September 2014 Anna-Leena Manninen

Abbreviations

3DRA	three-dimensional rotational angiography
N_A	Avogadro's constant
ABC	automatic brightness control
AEC	automatic exposure control
D	absorbed dose
BSF	backscatter factor
CTA	computed tomography angiography
CT	computed tomography
CTDI	computed tomography dose index
$CTDI_{vol}$	volume computed tomography dose index
$CTDI_W$	weighted computed tomography dose index
CV	coefficient of variation
DAP	dose area product
DLP	dose length product
DRL	diagnostic reference level
DSA	digital subtraction angiography
E_b	binding energy
E_k	kinetic energy
E	effective dose
ESD	entrance surface dose
ESE	entrance skin exposure
FOV	field of view
FDD	focus to detector distance
FSD	focus to skin distance
FGD-1000	dose measurement device type FGD-1000
GD-352M	glass dosimeter type no. 352M
H_T	equivalent dose
$K_{a,b}$	beam air kerma
$K_{a,i}$	incident beam air kerma
$K_{a,e}$	entrance surface air kerma
kVp	peak kilovoltage
LIH	last image hold
mAs	product of tube current (in milliamperage) and exposure time (in seconds)
MSCT	multi-slice computed tomography

OSLD	optically stimulated luminescence dosimeter
PMMA	polymethylmethacrylate
RPL	radiophotoluminescence
RPLD	radiophotoluminescence dosimeter
SID	source to image detector distance
TLD	thermoluminescence dosimeter
UAE	uterine arterial embolization
u_C	combined standard uncertainty
UV	ultraviolet radiation
T_f	fluoroscopy time
Z	atomic number
Z_{eff}	effective atomic number
σ_{pe}	atomic photoelectric effect cross section
σ_{incoh}	incoherent Compton effect cross section
μ/ρ	mass attenuation coefficient
μ_{tr}/ρ	mass energy transfer coefficient
μ_{en}/ρ	mass energy absorption coefficient

List of original publications

This thesis is based on the following publications, which are referred to throughout the text by their Roman numerals:

I Manninen AL; Koivula A; Nieminen MT (2012) The applicability of radiophotoluminescence dosemeter (RPLD) for measuring medical radiation (MR) doses. Radiat Prot Dosim 151(1): 1–9.

II Manninen AL; Ojala P; Nieminen MT; Perälä J (2014) Fetal Radiation Dose in Prophylactic Uterine Arterial Embolization. CardioVascular Intervent Radiol, 37(4): 942–948.

III Manninen AL; Isokangas JM; Karttunen A; Siniluoto T; Nieminen MT (2012) A Comparison of Radiation Exposure between Diagnostic CTA and DSA Examinations of Cerebral and Cervicocerebral Vessels. Am J Neuroradiol 33(11): 2038–2042.

Table of contents

1 Introduction

Ionization radiation has brought substantial benefits when used in medicine, but there are known risks due to stochastic effects and tissue reactions (deterministic effects) (UNSCEAR 2008, ICRP 2007, ICRP 2012, Holmberg *et al.* 2010a). The rapidly increasing collective and cumulative doses are partly caused by unnecessary and inappropriately optimized examinations, and partly by an increasing number of new medical applications, such as multi-slice computed tomography (MSCT), which produce better image quality and facilitate the diagnosis (Holmberg *et al.* 2010b). In 2011, the relative proportions of computed tomography (CT) examinations, angiographic examinations, fluoroscopy- and CT-guided interventional procedures in Finland were ca. 9%, 1% and 1%, respectively (STUK 2013). Fluoroscopy- and CT-guided interventional procedures increased by 24% during the years 2008-2011 (STUK 2013). Although these examinations account for a relatively small portion of all radiological examinations, they cause rather high organ doses in the 10–100 mGy range for an individual patient compared with other imaging modalities in radiology (Wall *et al.* 2006, McCollough *et al.* 2009). With interventional fluoroscopy procedures, the skin dose can be 2 Gy or even higher (IAEA 2007). However, the radiation risk is estimated to be negligible on equivalent doses less than 0.1 mSv, minimal 0.1-1 mSv, very low 1–10 mSv, and low 10–100 mSv (McCollough *et al.* 2009). There are specific groups of patients, such as children and pregnant women, which need particular radiation protection. The lifetime cancer risk for children is estimated to be about three times that of the population as a whole (ICRP 2007). Approximately 3–10% of various types of radiological examinations are performed on children aged 0–15 years (UNSCEAR 2013). In Finland, 9% of all X-ray studies are performed on children (STUK 2013). The individual justification and optimization of the procedure must be done before radiation exposure especially in the case of children and during pregnancy (Dauer *et al.* 2012). Furthermore, the estimation of the radiation exposure of the fetus is necessary if the fetus is in the direct beam or proximal to a scattered beam (IAEA 2007, Dauer *et al.* 2012).

Because the imaging techniques have very different irradiation geometries and the radiation exposure is reported in different quantities, the effective dose is a useful means of comparing the radiation exposure of different procedures, whereas the absorbed doses of organs predict tissue reactions (ICRP 2007). In radiology, three methods of patient dose assessment are used: (i) direct dose

measurement on a patient, (ii) dose measurements in physical phantom and (iii) Monte Carlo simulations. Lack of up-to-date dose information and conversion coefficient complicates the justification and optimization of the procedures. Choosing the best procedure for the diagnosis with the lowest radiation dose and cost is challenging (Mamourian *et al.* 2013).

Passive solid-state dosimeters can be used for direct dose measurement on a patient and in a phantom for a specific medical examination. The characteristics of the passive dosimeter are that the radiation induces ionization in the material, which is proportional to the energy absorbed in matter. Thermoluminescence dosimeter (TLD), optically stimulated luminescence dosimeter (OSLD), and radiophotoluminescence dosimeter (RPLD) are commonly used passive dosimeters (Riesen & Liu 2012). TLDs have been used more frequently for the past few decades for medical dosimetry (Bhatt & Kulkarni 2013). Some disadvantages of the TLDs, such as fading of the dose in room temperature and during the readout procedure and poor uniformity between dosimeter elements, have led to the development of methods for passive solid-state dosimetry (Oberhofer & Scharmann 1993, Moscovitch & Horowitz 2007). OSLD was first developed in the 1950s and further in the 1990s for environmental and personnel monitoring. The reusability and multiple reading procedures of OSLD materials are a result of more constant electron traps than in TLD materials (Riesen & Liu 2012). OSLD material is not sensitive to thermal energy, which liberates the trapped electron-hole pairs in TLD material. OSLD material has a small fading effect, better batch uniformity, reproducibility, and angular dependence than TLD materials (Riesen & Liu 2012). Electron-hole traps are liberated by light in OLSD material, whereas in TLD material, the stored energy is erased by heating (Riesen & Liu 2012). Because some OSLD materials are sensitive to visible light, they must be kept in light-tight containers (Riesen & Liu 2012). OLSD has good tissue equivalence and high sensitivity (Kurobori *et al.* 2014), but it has the disadvantage of energy dependence, depending on the material, and the same applies to TLD materials (Knezevic *et al.* 2013). Some OSLD materials underestimate radiation under 100 keV and are not suitable for dose measurements in radiology (Sommer & Henniger 2006, Riesen & Liu 2012, Bhatt & Kulkarni 2013). In RPLD materials, electrons which are transferred to the conduction band by ionizing radiation migrate to deep traps. These deep traps are earth or transition metal (i.e. silver) ions doped as impurities into the phosphate material. The proportioned trap can then be photoexcited without the electron being erased back into the conduction band (Riesen & Liu 2012). The main

difference to OSLD and TLD materials is that stable color centers in RPLD material can be repeatedly read out by photo excitation without fading in the signal per reading, whereas OSLD has some fading after a reading cycle (Jursinic 2007).

In the late 1950s, RPLD was developed by Schulman *et al.* 1951 for personnel monitoring mainly as an emergency dosimeter for civil and military use (Perry 1987). RPLD was used in radiation therapy dose measurements (Araki *et al.* 2003, Araki *et al.* 2004, Nakagawa *et al.* 2005, Takayuki *et al.* 2005, Takayuki *et al.* 2008, Rah *et al.* 2009a, Rah *et al.* 2009b, Mizuno *et al.* 2008, Rah *et al.* 2011) as well as personnel and environmental monitoring (Piesch *et al.* 1990, Hsu *et al.* 2006, Lee *et al.* 2009). Because the early RPLD materials were not sufficient for low-dose measurements, glass dosimeter material was developed further (Yokota & Muto 1971, Perry 1987, Huang & Hsu 2011). Early dosimeter reading technology was not able to measure low doses (Perry 1987, Piesch *et al.* 1990, Huang & Hsu 2011). The clinical applications of RPLD for patient radiation dose measurements in the energy ranges used in radiology are few for RPLD using energy compensation filter (Nishizawa *et al.* 2003, Matsubara *et al.* 2009, Knezevic *et al.* 2011) and for RPLD without energy compensation filter (Moritake 2008, Nishizawa *et al.* 2008, Hayakawa *et al.* 2010, Moritake *et al.* 2011, Matsubara *et al.* 2011, Kato *et al.* 2013, Sun *et al.* 2014).

The aim of this thesis was to assess the applicability of RPL dosimetry for dose determination in radiology. The various properties of RPLD were investigated for measuring radiation doses in air and on the surface of the phantom. The absorbed dose measurement was carried out through vaginal measurements in pregnant women undergoing fluoroscopy imaging during prophylactic catheterization before uterine artery embolization (UAE). The radiation exposure of two different types of angiography imaging methods was done by comparing the effective doses of CTA and DSA for a typical four-vessel angiography of the cerebral and cervicocerebral area, by using the same dose determination technique with RPLDs in an anthropomorphic phantom.

2 Review of the literature

2.1 Radiation dose assessment in radiology

Radiation is widely used in medicine for diagnostic and therapeutic applications. Dosimetry in radiology involves the application of various dose quantities, which are used for quality assurance purposes and for estimating patient dose. These quantities are determined in air or in phantom measurements using an ionization chamber or a TLD, RPL, semiconductor dosimeter, and radiochromic film (Riesen & Liu 2012). The application-specific dose quantities are useful for following up patient doses, and for optimizing the image protocols. The commonly used dose quantities for diagnostic reference levels (DRL) are dose area product (DAP), dose length product (DLP), and entrance surface dose (ESD), which is defined as entrance surface air kerma ($K_{a,e}$) (Toivonen & Komppa 2003, IEAE 2007).

The dose quantities used in the evaluation of tissue reactions and stochastic effects are the absorbed (D) and effective dose (E). Direct dose measurements are commonly used for superficial organs such as the eye, skin, thyroid, or testes on a patient or using an anthropomorphic phantom (UNSCEAR 2008). Passive solid-state dosimeters are used for this purpose because of their small physical size, high sensitivity, and usually low cost. The effective dose may be calculated from phantom measurements (Cohnen *et al.* 2006, Kawaura *et al.* 2006, Matsubara *et al.* 2009, McCollough *et al.* 2010, Struffert *et al.* 2014), or Monte Carlo results (Christner *et al*. 2010, McCollough *et al.* 2010), or by using a conversion coefficient (Huda *et al.* 2008 Christner *et al*. 2010). In fluoroscopy and angiography procedures, Monte Carlo simulation is difficult to apply due to the varying location of the field of view (FOV) relative to the position of the patient. Furthermore, the beam output varies due to the patient size, chosen FOV size, the varying focus detector distance, and projection used when automatic exposure control (AEC) is applied. Nevertheless, both Monte Carlo and phantom simulations have limitations due to the difficulty to determine the exact location of the organ or to position the dosimeters so that the setup corresponds to the dose of the whole volume of the organ. Because the examinations in radiology usually result in a limited irradiation of the body and the doses delivered are relatively low, a required accuracy of 20% with 95% confidence limit for adults is sufficient for radiation risk assessment (IAEA 2007). Estimating the relative radiation risks

for comparative dose measurements and for cases where tissue reactions are expected, an uncertainty of 7% is appropriate. An uncertainty of 7% in dosimeter reading is sufficient for assessing the potential risk of pediatric examinations (IAEA 2007). The overall uncertainty of a dose measurement in radiology for TLD is recommended to be $\leqslant$ 12.5 % (Zoetelief *et al.* 2000). This gives the relative expanded uncertainty of 25% at the 95% confidence interval. For diagnostic dosimeters, the relative expanded uncertainty of measurement is adopted to be 20% (IAEA 2007).

2.1.1 Interaction of radiation with matter

Radiation dose detection in a dosimeter is based on the interaction of the radiation in the matter. The dosimetric properties are related to the particular interaction phenomenon. The characteristics of the detector material must be close to the scattering and absorbing properties of the tissue. The energy of radiation sets electrons in motion, producing ionization of the atoms or molecules in the medium (Dendy & Heaton 1999). The interaction of the radiation in the matter is dependent on the density, the atomic number (Z) of the absorption medium, and the photon quantum energy ($E=hv$). Typically, the interaction phenomena which transfer energy to the medium are photoelectric absorption and Compton scattering in the X-ray energy range used in radiology (Dendy & Heaton 1999). The contribution of Coherent scattering including Thomson and Rayleigh scattering is 5–10% of the other basic interactions. Coherent scattering does not transfer energy to the medium and thus cannot produce ionization (Curry *et al.* 1990, Dendy & Heaton 1999). Coherent scattering is excluded from the current examination due to its insignificant role in radiation protection in radiology. Pair production is dominant in the radiation therapy energy ranges and it is nonexistent at X-ray energies in radiology (Curry *et al.* 1990).

In the energy range used in radiology, total atomic cross section (σ_{tot}) is the sum over cross sections for the most probable individual processes by which photons interact with atoms and is derived as

$$\sigma_{tot} = \sigma_{pe} + \sigma_{incoh} \tag{1}$$

where σ_{pe} is the atomic photoelectric effect cross section and σ_{incoh} is the incoherent Compton scattering cross section (Hubbell 1999). The mass attenuation coefficient (μ/ρ) is derived from the interactions between incident

photons and matter, which accounts for the density of the material where interactions occur and is defined as

$$\frac{\mu}{\rho} = (\sigma_{pe} + \sigma_{incoh})/uA \quad (2)$$

where μ is the linear attenuation coefficient in and ρ is the density of the element. u is the atomic mass unit ($1.6605402 \times 10^{-24}$g) and A is the gram atomic or molecular weight of the element (Hubbell 1999). The quantification of the mass attenuation coefficient μ/ρ can be defined as

$$\frac{\mu}{\rho} = t^{-1}\ln(\frac{I_0}{I(t)}) \quad (3)$$

where t is the mass thickness of the absorber layer, I_0 is the intensity of the incident beam of photons measured without absorber, and $I(t)$ is the intensity of the transmitted beam measured with absorbed layer (Hubbell 1999).

Photoelectric effect

The photoelectric effect is predominant at photon energies less than 30 keV with body tissue. The probability of the photoelectric effect increases sharply as Z increases. The photoelectric mass attenuation coefficient (μ/ρ) for the energy region about 0.1 MeV and below is defined as

$$\frac{\mu}{\rho} = \left(\frac{Z}{h\nu}\right)^3 \quad (4)$$

(Attix 2004, Curry *et al.* 1990). The interaction occurs usually with the most tightly bound electron in the K-shell of the atom orbit, and binding is greater for atoms of high Z. The photoelectric effect is most probable when an incident photon has a little more energy than the binding energy of the K-shell electron. The photon energy ($h\nu$) is able to eject the electron from its orbit, giving up all its energy to overcome the binding energy (E_b) of the electron and producing a photoelectron (Figure 1) whose kinetic energy (E_k) is

$$E_k = h\nu - E_b \quad (5)$$

(Attix 2004). The ejected photoelectron spends its energy close to its original location, and therefore the energy imparted from the photon to this electron is directly proportional to the absorbed dose of matter (Dowsett *et al.* 2006). The residual atom is left in a highly excited state since there is a vacancy in one of its

orbital electron shells. The vacancy in the K-shell will be filled by an L-shell electron emitting a characteristic photon, whose energy is

$$E = E_1 - E_2 = hv = \frac{hc}{\lambda} \quad (6)$$

where E_1 is the binding energy of the K-shell electron and E_2 is the binding energy of the L-shell electron, see Figure 1. The number of photons emitted is proportional to the number of primary vacancies created in the atomic electron shells, and is known as the fluorescence yield (Dendy & Heaton 1999). The production of the Auger electrons released from the outer shell of the atom due to the characteristic photons (see Figure 1) is more probable with low Z atoms and with low energy ranges. The result is that the total amount of the energy of the initial photon is absorbed in the matter. All the atoms with low Z are capable of interacting through the photoelectric reaction due to low K-shell binding energy. At low photon energies, the photoelectric interaction is predominant in the energy transferred to the secondary electrons (Dendy & Heaton 1999).

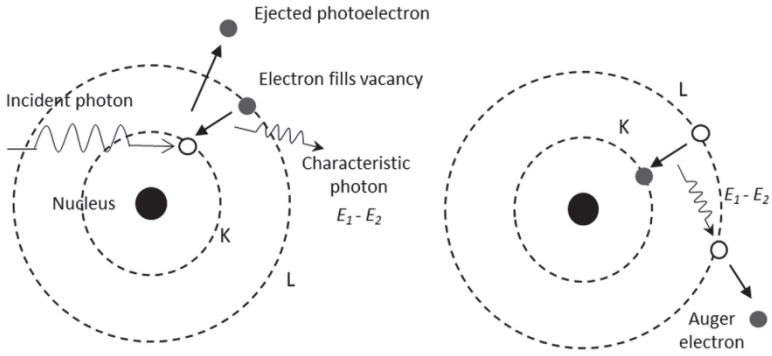

Fig. 1. Schematic representation of the photoelectric effect and forming of an Auger electron.

Compton effect

The most important interaction between X-rays and body tissue is inelastic Compton scattering. It is more probable to occur with low Z atoms when the radiation energy exceeds 30 keV. The probability of the Compton effect depends on the photon energy, absorber density, and the total number of electrons in an absorber regardless of the element atomic number (Attix 2004). The mass attenuation coefficient (μ/ρ) for the Compton effect is defined as

$$\frac{\mu}{\rho} = \frac{N_A Z}{A}\sigma \tag{7}$$

where N_A = 6.022 x 10^{23} mol^{-1} is Avogardro's constant, the number of atoms or molecules in mole of any element, Z is the atomic number, A= gram atomic or molecular weight of the element, ρ= density in g/cm^3, and N_AZ/A= number of electrons per gram of material and σ= cross section per electron (Attix 2004, Curry *et al.* 1990).

The incoming photon transfers a portion of its energy (hv) to the unbound outer shell electron, which is then known as a recoil electron or Compton electron. After the collision, the electron departs at angle (θ) with kinetic energy (E_k). The photon scatters at angle (φ) with lower quantum energy (hv') (see Figure 2). The kinetic energy of the electron is expressed as

$$E_k = hv - hv' \tag{8}$$

The energy of the original photon (hv) along direction ($0°$) can be expressed as

$$hv = hv' \cos\varphi + pc\cos\theta \tag{9}$$

where p is a momentum of the electron and c is the speed of light. The phenomenon is one of scatter and partial absorption of energy (Attix 2004).

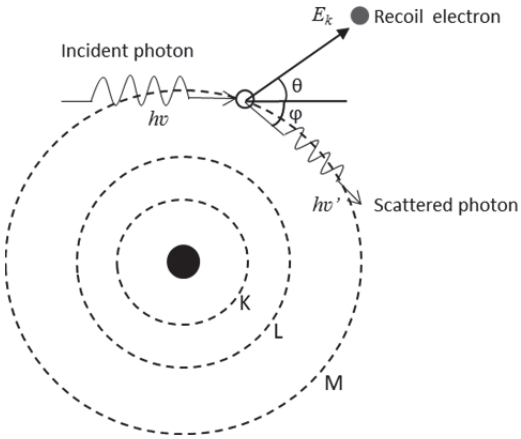

Fig. 2. Schematic representation of the Compton scattering.

The kinetic energy of the electron is rapidly dissipated by ionization, excitation, and as heat in the medium. When the photon is scattered through angle φ, the change in energy ΔE is given by

$$\Delta E = (E^2/m_e c^2)(1 - \cos\varphi) \tag{10}$$

The scattered photon with lower energy continues in a deflected direction in the material (Attix 2004). When a low-energy photon undergoes Compton interaction, only a small fraction of the energy of the incident photon is transferred to the electron, whereas a high-energy photon gives up most of the energy to the Compton electron. The transfer of energy to the Compton electron is small in the energy range used in radiology (Dendy & Heaton 1999, Dowsett *et al.* 2006).

Radiation energy absorption in medium

The absorbed dose D is defined as

$$D = \frac{\mathrm{d}\varepsilon}{\mathrm{d}m} \tag{11}$$

where dε is the mean energy imparted to matter of mass dm (IAEA 2007).

The mass energy absorption coefficient (μ_{en}/ρ) is a measure of the average fractional amount of incident photon energy transferred to the kinetic energy of charged particles as a result of these interactions. The kinetic energy of the charged particles given by the incident photon is the approximation of the absorbed dose imparted into the matter (Toivonen & Komppa 2003). The mass energy absorption coefficient (μ_{en}/ρ) is related to the mass energy transfer coefficient (μ_{tr}/ρ) through association

$$\frac{\mu_{en}}{\rho} = (1 - g)\frac{\mu_{tr}}{\rho} \tag{12}$$

where μ_{tr}/ρ is the sum of the kinetic energies of all those primary charged particles released by photons per unit mass (IAEA 2007, Toivonen & Komppa 2003). The μ_{tr}/ρ includes the energy of the secondary electrons' conversion into bremsstrahlung photons and is expressed as parameter g. In X-ray energy range, the value of g is insignificantly low, typically less than 0.001 (Toivonen & Komppa 2003). The conversion between the air kerma (K_a) and absorbed dose to air is then 1.00. The dosimetric quantity K_a is given as

$$K_a = \Psi\frac{\mu_{tr}}{\rho} \tag{13}$$

where ψ is the photon energy fluence and is defined as

$$\Psi = \Phi E \tag{14}$$

where Φ is the photon fluence and E the photon energy (Hubbell & Seltzer 1996). The absorbed dose in specified material is defined as

$$D = \Psi \frac{\mu_{en}}{\rho}. \quad (15)$$

(Toivonen & Komppa 2003). In patient dosimetry, absorbed dose to air (D_a) or absorbed dose to tissue (D_t) is used in many applications. D_t is defined as

$$D_t = D_a \frac{(\mu_{en}/\rho)_t}{(\mu_{en}/\rho)_a} \quad (16)$$

(Hendee & Ritenour 2002, Toivonen & Komppa 2003). The absorbed dose to tissue is related to absorbed dose in air through multiplication of the ratio of the mass energy absorption in medium to that in air. The conversion factor of this ratio is 1.04–1.07 for diagnostic X-ray qualities of 50–150 kV tube voltages and 1–10 mm for Al HVL values (Seuntjens *et al.* 1987) and 1.00–1.06 for 50–130 kV 2.3–10.8 mm Al HVL (Benmakhlouf *et al.* 2011).

Interaction of X-rays with body tissues

In a pure material, the atomic number is defined as the number of protons found in the nucleus of an atom. In an atom of neutral charge, the atomic number is also equal to the number of electrons. When ionization radiation interacts with a complex medium, the molecular grouping has an impact on the absorption of the photon energy in the medium. In composite material, the effective atomic number (Z_{eff}) is used instead of the atomic number (Z) (Shivaramu 2002). The effective atomic number varies with photon energy and is calculated as

$$Z_{eff} = (\sum a_i \, Z_i^n)^{\frac{1}{n}} \quad (17)$$

where a_i is the electron fraction of the element, Z_i is the atomic number of the element, and n is the variable exponent which varies from 2.94 to 3.4 due to the elements and their molecular grouping (Perry 1987).

The human body can be modeled by three different body tissues (see Figure 3 A). They are muscle, fat, and bone (Hendee & Ritenour 2002). The element composition of soft tissues, such as collagen, internal organs, ligaments, blood and cerebrospinal fluid, is close to the element composition of muscle. Soft tissue is approximately 75% to 100% water (Hendee & Ritenour 2002). Breast tissue was modeled by fat. Fat was used in calculations to improve the accuracy of doses instead of using soft tissue material (Jones 1997). Fat has a greater concentration of low Z elements than soft tissue. Therefore, fat has a lower density and effective atomic number compared with muscle and other soft tissues.

The effective atomic number for fat is 5.9–6.3, for soft tissue and water 7.4, for air 7.6, and for bone 11.6–13.8 (Hendee & Ritenour 2002).

The dosimeter used in the dose measurements must be calibrated against the reference dosimeter in air, because air is accepted as a reference material with its sufficient approximation to soft tissue, $(\mu_{en}/\rho)_{t/a}$ (Perry 1987) (see Figure 3 B).

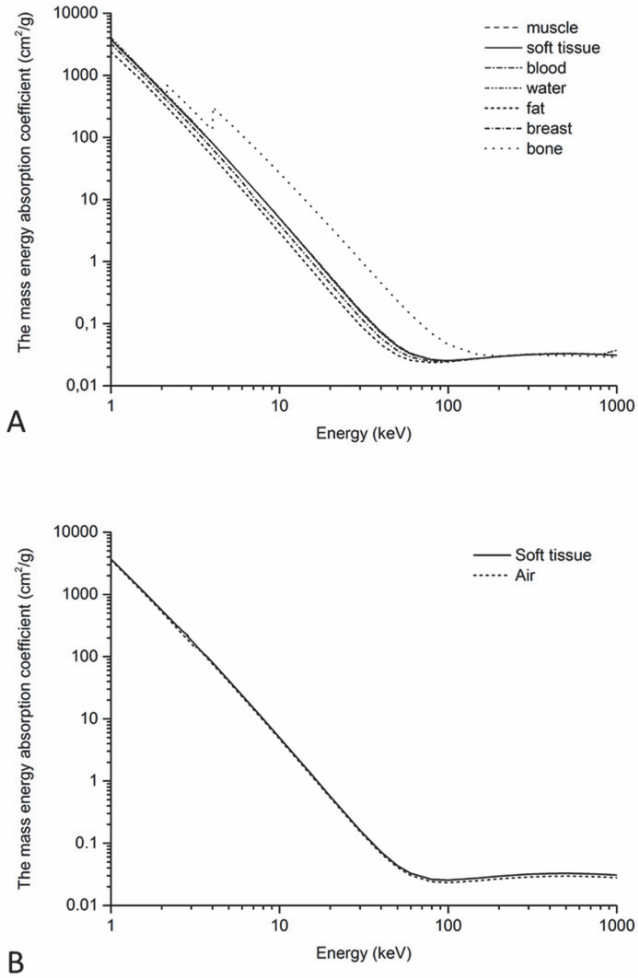

Fig. 3. A) The mass energy absorption coefficients for different tissues and B) for soft tissue and air. Produced from NIST Standard Reference Database, 126 NISTIR 5632 (Hubbell & Seltzer 1996).

2.1.2 Application-specific dose quantities

Dose-area product

Dose-area product (*DAP*) is defined as the integral of the air kerma (K_a) over the area (A) of the X-ray beam in a plane perpendicular to the beam axis and is expressed as

$$DAP = \int_A K_{a,b}(x,y)dxdy \tag{18}$$

where A is the apparent beam area measured at the same distance as $K_a(d\ )$ (Toivonen & Komppa 2003).

The patient's total dose from several projections is determined by using a DAP meter, which is a large-area transmission ionization chamber mounted on a diaphragm housing to intercept the entire cross-section (Toivonen & Komppa 2003). Modern X-ray equipment calculate the DAP value internally using exposure factors, such as peak tube voltage (kVp), a measure of electric charge obtained by multiplying the electric current in milliamperage by the time in seconds (mAs), the position of the beam relative to the patient and the field of view (FOV), and collimation used (Zoetelief *et al.* 2000). DAP is not a very good metric for estimating interventional radiation exposures. Especially, it is a poor estimate of the tissue reactions (see 2.1.3), such as high local skin dose due to the varying location of the FOV relative to the skin and the fact that it does not account for backscatter. DAP is a better quantity for estimating the stochastic effect (see 2.1.3) (Toivonen & Komppa 2003, IAEA 2007).

Entrance surface air kerma

Entrance surface air kerma ($K_{a,e}$) is equal to the product of the backscatter factor (BSF) and $K_{a,i}$, for a single projection. Incident beam air kerma ($K_{a,i}$) is expressed as

$$K_{a,i} = K_{a,b}(d_{FS}) = K_{a,b}(d)\left(\frac{d}{d_{FS}}\right)^2 \tag{19}$$

where d_{FS} is the focus-to-skin distance and beam air kerma $K_{a,b}(d)$ is the transfer of radiation energy from photons to the kinetic energy of secondary ionizing particles of secondary electrons in the air at the central axis of the beam at distance d, excluding the contribution from backscattering (Toivonen & Komppa

2003). Backscatter is radiation deflected by scattering processes from the target element in direction of 90 degrees or greater compared with the original direction of the beam of radiation. The amount of backscatter can be 19–57% depending on the X-ray spectrum, the X-ray field size, and the thickness of the patient or phantom (Ma & Seuntjens 1998, Benmakhlouf *et al.* 2011, Benmakhlouf *et al.* 2013). Backscatter factor (BSF) is a correction factor for converting incident air kerma to entrance surface air kerma. BSF is needed for the determination of local skin doses, particularly in interventional radiology. Typical BSF values for radiology dosimetry in different body parts have been determined using Monte Carlo simulation (Petoussi-Henss *et al.* 1998, Benmakhlouf *et al.* 2011).

Metrics for exposure in fluoroscopy procedures

For radiation dose estimation in fluoroscopic procedures, special metrics have been developed, such as reference point air kerma (*reference dose*), peak skin dose, and entrance surface air kerma rate and fluoroscopy time (Miller *et al.* 2010). Entrance surface exposure (ESE) is used in the same meaning as reference point air kerma in the present study. Entrance surface air kerma is measured directly on a phantom or calculated from the incident air kerma using BSF (IAEA 2007). When using dosimeters of small volume in direct $K_{a,e}$ measurement, the error in backscatter detection can be minimized by shortening the distance between the effective center of the dosimeter and the surface of the target (Zoetelief *et al.* 2000).

An interventional reference point has been defined in standard IEC 60601-2-43 to represent the typical focus to skin distance, independently of the projection. For isocentric X-ray systems, this point is 15 cm from the isocenter in the direction of the focal spot (Chida *et al.* 2010a, Miller *et al.* 2010, Chida *et al.* 2011). A comparison of displayed reference dose to the actual measured value was investigated and the difference was approximately 15%, because the reference point deviated from the IEC 60601-2-43 standard among the compared fluoroscopy equipment (Chida *et al.* 2011). The beam air kerma $K_{a,b}(d_{ref})$ at the focus to reference point distance (d_{ref}) is an approximation of the incident beam air kerma and can be calculated as

$$K_{a,i} \approx K_{a,b}\left(\frac{d}{d_{ref}}\right)^2 \tag{20}$$

(Toivonen & Komppa 2003).

Peak skin dose measured in grays is the highest radiation dose, $K_{a,e}$ including backscatter at any portion of a patient's skin during a procedure. In practice, peak skin dose can be determined by solid-state dosimeters on the patient's skin. This quantity is closely related to deterministic skin effects (Zoetelief *et al.* 2000, Miller *et al.* 2010). Reference dose is an approximation of the maximum skin dose, because the X-ray beam is moved periodically with respect to the patient and is directed at different areas of the patient's skin. This approximation of skin dose overestimates the likelihood of deterministic effects. Fluoroscopy time does not correlate very much with the other dose metrics used in fluoroscopy (Miller *et al.* 2010).

Computed tomography dose index and dose length product

The computed tomography (CT) dose index (CTDI) was developed as a metric to quantify the radiation output from a CT examination. CTDI reflects the average dose to a cylindrical phantom and does not reflect the dose in the particular patient (McCollough *et al.* 2011). A phantom with a 16 cm diameter is used to determine the scanner output for head examinations and a phantom with a 32 cm diameter is used for body examinations. Both phantoms are 14–15 cm long (McCollough *et al.* 2011). Due to the attenuation of the radiation, the absorbed dose varies across the axial plane of the cylindrical phantom. Therefore, dose measurements are made at the center and at the periphery one centimeter deep from the surface in the phantom, and a weighted average is calculated as

$$CTDI_w = \frac{1}{3}\, CTDI_{100,center} + \frac{2}{3} CTDI_{100,edge} \tag{21}$$

where $CTDI_{100}$ is accumulated multiple scan dose at the center of a 100 mm integrated dose length determined by a pencil-shaped ionization chamber of 100 mm length and is defined as

$$CTDI_{100} = \frac{1}{NT} \int_{-50mm}^{+50mm} D(z)dz \tag{22}$$

where *D(z)* is the single rotation dose profile along the z-axis (AAPM 2008).

The volume CTDI ($CTDI_{vol}$) is displayed on the scanner console. $CTDI_{vol}$ represents the average absorbed radiation dose over the x, y, and z directions (AAPM 2008). The $CTDI_{vol}$ is a standardized measure of the radiation output of a CT system and represents the dose for a specific scan protocol, which almost always involves a series of scans. $CTDI_{vol}$ is defined as

$$CTDI_{vol} = \frac{NT}{I} CTDI_W \quad (23)$$

where I is the table increment per axial scan (mm). Since pitch is defined as the ratio of the table travel per rotation (I) to the total, nominal beam width (NT), $CTDI_{vol}$ can be expressed as

$$CTDI_{vol} = \frac{1}{pitch} CTDI_W. \quad (24)$$

$CTDI_{vol}$ is used for calculating the dose length product (DLP), which is a parameter reflecting the total radiation exposure of a patient for computed tomography study. DLP is expressed as

$$DLP = CTDI_{vol} scan\ length \quad (25)$$

(AAPM 2008).

2.1.3 Quantities for estimating stochastic effect and tissue reactions

When assessing the radiation exposure of the patient, the organ and effective dose (E) must be determined. Direct dose measurements of the organs are usually unavailable when patients undergo X-ray examinations. In phantom measurements, an anthropomorphic phantom can be used for the dose estimation of organs.

Determination of the mean absorbed dose of the organ and the equivalent dose

The radiation effect depends on the amount of energy and the type of radiation a tissue is exposed to. The absorbed doses of organs predict tissue reactions such as a temporary epilation, hair loss, or opacity of the lens. Such tissue reactions have a dose range, where the severity of the harm will increase. The harm will be certain when the dose or the dose rate is high enough (ICRP 2012). The tissue reactions are rare in diagnostic radiology, but in special circumstances they may occur when the local dose is very high. The most important example is the high skin dose, which can rise during interventional procedures using X-rays (Miller *et al.* 2010). The largely used entrance skin dose (ESD) can be defined through the entrance surface air kerma including BSF. ESD is used for determining the deterministic effects on the skin. Direct ESD measurement can be determined e.g. by laying a solid-state dosimeter on the entrance surface of a phantom or a

patient's skin (Zoetelief *et al.* 2000). The absorbed dose is numerically equal to the equivalent dose (H_T) for X-rays and is calculated from the average of the dose which has absorbed into an organ and is defined as

$$H_T = \sum_R W_R D_{T,R}, \text{with } W_R = 1 \quad (26)$$

where W_R is the radiation weighting factor, expressing the biological effect of a given type of radiation, and $D_{T,R}$ is the absorbed dose measured in tissue (T) with radiation (R) (IAEA 2007).

H_T of radiation-sensitive organs and tissues is determined when assessing the stochastic effect of the radiation exposure. Because some tissues are distributed throughout the body, the calculation of H_T is challenging. For example, mean skin dose is the mean absorbed dose to the whole skin, in the meaning of organ or tissue dose; the mean value of local skin dose over the total body (Toivonen & Komppa 2003). Other tissues distributed in the same way are active bone marrow, bone surface, muscles, lymphatic nodes and colon.

The mass of the active bone marrow and distribution through the skeleton depend on the patient's age. According to the experimental data of Hudson (1965), the quantitative estimates of the regional distribution of active bone marrow in infants and children are 29.5% in the skull and 23.7% in the lower limbs, whereas in adults the figures are 8.3% and 5.6%, respectively. In adults, 19.2% of active bone marrow is located in the ribs and sternum, 29.9% in the spine and 33.3% in the pelvis (Cristy 1981, Cristy & Eckerman 1987). The fractional masses of bone marrow in the different regions of the skeleton must be taken into consideration when calculating the equivalent dose of the active bone marrow (Cristy & Eckerman 1987).

There are several methods to determine the mass of active bone marrow (Hough *et al.* 2011). The total active bone marrow mass in a body differs by less than 4% between methods, whereas the active bone marrow mass of different bone areas can vary 20–45% between methods (Caracappa *et al.* 2009). It is assumed that the marrow absorbs energy per gram as efficiently as bone. This is correct at 200 keV or more, but at energies below 100 keV, it overestimates the dose to marrow due to the photoelectric effect of the photon interaction process of the bone tissue (Cristy & Eckerman 1987).

The approximation of the dose in lymphatic nodes can be calculated as sum of the weighted average dose for several surrogate organs and tissues. The dose in colon can be calculated as the mass-weighted average of the upper large intestine and the lower large intestine (Tapiovaara & Siiskonen 2008). The estimation of

the radiation dose of muscles can be determined from the doses in surrounding organs weighted by the dimension of the irradiated area (Ludlow *et al.* 2006).

Determination of effective dose

When evaluating the stochastic effect due to the radiation dose, the likelihood of the harmful effect must be determined. The stochastic effects are manifested as cancer induction, malignant disease, or heritable effects caused by an exposure to ionization radiation. The fatal cancer risk averaged over a typical population is estimated to be 5% per Sv (ICRP 2007). If the patient is an infant, the fatal cancer risk would be about three times higher, whereas for an old person the corresponding risk may be a factor of three times lower than the typical population-averaged risk (ICRP 2007).

Active bone marrow, colon, lungs, stomach, breasts, and 'remainder tissues' are the tissues of the human body that are most sensitive to ionizing radiation and are weighted highly for stochastic effect estimation. The radiation exposure of active bone marrow is associated with radiation-induced leukemia. The other organs are associated with solid tumors (ICRP 2007).

This different sensitivity to stochastic radiation damage is considered by the tissue weighting factors (Table 1), which estimate the probability for the occurrence of stochastic effects in various organs and tissues (ICRP 2007). Effective dose (E) is the sum of the weighted equivalent doses (H_T) in all organs and tissues of the body, and is defined as

$$E = \sum_T W_T H_T, \text{with } \sum W_T = 1 \tag{27}$$

where W_T are dimensionless tissue weighting factors characterizing the relative sensitivity of various tissues with respect to cancer induction and heritable disease (ICRP 2007).

Table 1. Tissue weighting factors (ICRP 2007).

Tissues	W_T	$\sum W_T$
Active bone marrow, colon, lungs, stomach, breasts and remainder tissues[1]	0.12	0.72
Gonads	0.08	0.08
Bladder, esophagus, liver and thyroid	0.04	0.16
Bone surface, brain, salivary glands and skin	0.01	0.04
Total		1

[1]Remainder tissues: Adrenals, extrathoracic region, gall bladder, heart, kidneys, lymphatic nodes, muscle, oral mucosa, pancreas, prostate (male), small intestine, spleen, thymus and uterus/cervix (female)

In radiological studies, the patient's radiation exposure is unevenly distributed in the body, and a specific parameter is needed to represent the stochastic effect. The effective dose (E) is a method for comparing the stochastic effect from different diagnostic procedures (McCollough *et al.* 2010). Also, E serves as a tool to compare the radiation exposure of similar technologies and procedures in different hospitals, and furthermore, in comparison between different technologies used for the same radiation examination. However, E cannot be used to provide quantitative radiation risks for any one individual or subpopulation, because individual sensitivity to radiation effects or age- and sex-dependent weighting factors have not been determined by ICRP (Tapiovaara & Siiskonen 2008, McCollough *et al.* 2009, ICRP 2007)

2.1.4 In vivo absorbed dose determination

In vivo measurements during patient exposure are used when a maximally accurate dose is needed from a certain examination or treatment. Doses at depth are difficult, if not impossible, to obtain without invasive procedures. *In vivo* measurements are used to verify the dose planning in radiation therapy. Also, they may be used to determine radiation injuries in interventional treatments such as ESD measurements of the skin, lens of the eyes, thyroid, and testis (Moritake *et al.* 2008, Rah *et al.* 2011, Kato *et al.* 2013).

Intracavity dose measurements are not very commonly used. If the dosimeter is inserted inside a catheter of a suitable diameter, it can be used to reach organs such as ureters, renal pelvis, bronchial tree, uterus and blood vessels. This method can be exploited using RPLD in complex radiation therapy situations to check the accuracy of the treatment plans (Perry 1987, Takayuki *et al.* 2008). Intravaginal

dose measurements were previously done using the passive solid-state thermoluminescent dosimeter with uterine artery embolization for leiomyomas (Nikolic *et al.* 2000, Nicolic *et al.* 2001, Glomset *et al.* 2006,). Passive solid-state dosimeters are superior to semiconductors in this case since they do not have to be connected to an electrometer with cables during irradiation. Also, the X-ray positive material and small volume of the dosimeter are suitable for intracavity dose measurements. The dosimeter should be equivalent to tissue with regard to its absorption properties and it should not prevent diagnosis by modifying the radiation field or degrading the image quality. In addition, inertness to environmental factors and body contaminations such as humidity, temperature variations and light is required (Perry 1987).

2.1.5 Dose determination using phantoms

Polymethylmethacrylate (PMMA) phantoms of varying thickness and size are used for calibrating dosimeters or for quality assurance (QA) in radiology. PMMA is a material which has the same absorption and scattering properties as soft tissue and it is generally used as a patient model in tests used in radiation measurements in radiology (Hubbell & Seltzer 1996).

Anthropomorphic phantoms (for example Alderson-Rando Phantom), which are manufactured to simulate human physical characteristics, such as soft tissue, skeleton, and lung tissue, are widely used to determine the absorbed dose of organs and for assessing the effective dose.

2.2 Imaging methods in interventional radiology and diagnostic angiography

2.2.1 Fluoroscopy imaging

Fluoroscopy is a common technique used by clinical physicians to obtain real-time images of moving body parts and internal structures of a patient compared to static radiographic examinations. New-generation fluoroscopy equipment with pulsed fluoroscopy and a flat panel detector using automatic brightness control, last image hold technique, and image processing system ensure superior image quality while keeping the radiation dose for the patient reasonably low (Chida *et al.* 2010b). All modern fluoroscopy equipment have an automatic brightness

control (ABC) that adjusts peak tube voltage (kVp) and the amount of current (mA) flowing in the X-ray tube circuit. ABC ensures appropriate noise level, image contrast, and brightness when patient thickness varies. If thickness increases, kVp is increased to give a more penetrating beam. The ABC system reduces the tube current when maximum tube voltage is reached. The peak tube voltage can be fixed to the optimum spectrum for the K-edge of the contrast medium or catheter used. If the tube voltage is fixed at the optimum of the contrast medium, the increase in patient thickness is compensated by an increase in the tube current. Higher tube current reduces noise and improves image quality resulting in higher dose (Strauss 2006). These fluoroscopy imaging parameter settings are dependent on the used fluoroscopy equipment.

If there is a possibility to use pulsed fluoroscopy with low pulse frequency, e.g. 4 or 7.5 pulses per second, it has a significant effect on exposure; the absorbed dose is linearly proportional to the number of pulses per second (Dowsett *et al.* 2006). The dose is also dependent on the experience of the radiologist: the operator can minimize the dose by keeping the fluoroscopy time short, by using pulsed fluoroscopy, and using the last image hold (LIH) method (Mahes 2001, Chida *et al.* 2010b, ICRP 2010). In addition, dose reduction is possible by using maximal focus-to-skin distance and positioning the detector close to the patient, by avoiding magnification, by collimation to reduce the volume of tissue exposed to radiation, and by using additional tube filtration (Mahes 2001, ICRP 2010, Chida *et al.* 2010a).

Fluoroscopy-guided endovascular treatment is an alternative to surgery. In fluoroscopy guidance, a catheter is threaded through the vascular system to the area of interest after injecting contrast medium directly into arteries, immediately followed by the intervention, i.e., angioplasty, stenting, or embolization. These invasive endovascular procedures have already been used for decades with promising results. In addition, as a safe treatment, it is less invasive and has a lower risk compared to surgery. Shorter hospital stay and recovery reduce the costs of the treatment. Endovascular treatment is also an alternative for patients who cannot go through surgical treatment (Ohki & Veith 2000, Hanch *et al.* 1999). When using the optimized low-dose fluoroscopy method without angiography exposure, the patient exposure during endovascular treatment remains reasonably low (Andrew & Brown 2000).

2.2.2 Angiographic methods for vessel imaging

Angiography is defined as radiographic imaging series of vessels following the injection of contrast medium. Angiography serves to investigate normal and pathological states of the vessel system, particularly luminal narrowing and obstruction or aneurysmal widening. Traditionally, the imaging of the vessels has been carried out by digital subtraction angiography (DSA) using the angiography equipment of a C-arm system. The development of fast-volume scanning by spiral CT led to the development of computed tomography angiography (CTA). Also, imaging techniques such as magnetic resonance angiography (MRA) or ultrasound are important applications for imaging vessels (Kalender 2011). The current study deals with the first two angiography methods using ionization radiation.

Digital subtraction angiography

In digital subtraction angiography (DSA), consecutive images of the same region are acquired in rapid succession, before and after injection of a contrast medium. The mask or non-contrast image is taken before the contrast medium has reached the target area (Dowsett *et al.* 2006). Here, two frames are acquired; the first one to stabilize exposure factors, the second is for the mask image. Some applications use more frames to improve image quality by summing the frames for noise reduction (Dendy & Heaton 1999). In this image, normal anatomy is shown and stored on a computer. The contrast image is taken when the vessels have been filled with contrast agent. This image shows the filled vessels superimposed on normal anatomy and is stored on a computer. After the imaging of both images, logarithmic subtraction removes all anatomy of the target except the contrast medium-filled vessels, creating a third image. The vessel-to-background ratio is enhanced in DSA due to the subtraction technique, eliminating undesirable image information (Dowsett *et al.* 2006). The digital imaging allows high spatial resolution due to small pixel size and the possibility of automatic pixel shift. Improved temporal resolution is a result of the localization of an object in time from frame to frame and follows its movement. Using the automatic exposure control (AEC) sets the dose level of the exposure required for an adequate image. (Dowsett *et al.* 2006).

DSA has proven especially useful in the identification of vascular abnormalities, including occlusions, stenosis, ulcerated plaques, and aneurysms.

Intra-arterial DSA is considered superior to MSCT in accurately predicting degrees of stenosis (Psychogios *et al.* 2013). Also, DSA is used for various treatments, such as placement of stents or angioplasty angiography (Cloud & Markus 2003). Radiation exposure varies depending on the subtraction method selected for the examination and the number of views required for diagnosis. Despite its invasive nature, DSA is still generally considered the gold standard in the imaging of vessels (McKinney *et al.* 2008).

Computed tomography angiography

With computed tomography angiography (CTA), invasive catheterization is not needed; the contrast medium is given using a simple injection in the arm. CTA uses a computed tomography (CT) scanner to create images of blood vessels. While DSA is used for various treatments, non-invasive CTA is increasingly used for diagnostic purposes. MSCT technology with superior imaging quality has been developed for angiographic procedures thanks to increased scan speed and improved spatial resolution (Teksam *et al.* 2004, Teksam *et al.* 2005, Klingebiel *et al.* 2008).

Because CT is associated with high radiation dose, technical approaches have been developed for patient dose reduction. Formerly, the tube current was kept constant during the scan causing variable image quality. Anatomy-adapted tube current modulation has been a significant technical approach for dose reduction. The development of automatic tube current modulation techniques allows the tube current to be automatically adjusted during a CT examination, resulting in lower doses (Kalender 2011). To provide lower patient doses and constant image noise, the characteristics of angular and Z-axis modulation have been developed. Angular modulation adjusts the tube current within a single rotation of the X-ray tube. The tube current is increased in areas of higher attenuation, such as the lateral view through the shoulders, and decreased in areas with lower attenuation, such as anterior-posterior AP views through the chest. In addition, some CT scanners use projection-based real-time tube current modulation on the attenuation calculated from the previous rotation (Kalender 2011).

CTA aimed at imaging the head and neck area sets particular requirements for the imaging technique. Exact time matching of the time windows for contrast enhancement and scanning is challenging. The arrival time of the contrast agent can be determined by test bolus and repeated low dose scans of a single slice. Alternatively, the arrival of the actual bolus is possible to carry out by sequential

scans of a single slice and by switching to volume scanning after detecting its arrival (Kalender 2011). This conventional CTA method has the disadvantage of false-negative findings related to aneurysms located near to or within the skull base (Tomandl *et al.* 2006) and evaluating extracranial internal carotid artery aneurysms (Zhang *et al.* 2010). A method for eliminating bone to increase the sensitivity of CTA is needed (Tomandl *et al.* 2006).

Bone-subtraction CTA (BSCTA) uses a (low-dose) non-enhanced scan to create a bone model, and a contrast-enhanced scan for visualizing the vessels is acquired after it. The BSCTA image is then subtracted from the CTA data. Motion within the scans or between the non-enhanced and contrast-enhanced scans is a major problem for subtraction procedures. The increase of the dose due to non-enhanced scan is 27% (Lell *et al.* 2007). A new application of a single-acquisition contrast-enhanced dual energy CTA is reported to be a useful tool for evaluating intracranial aneurysms at a much lower radiation dose than digital subtraction CTA (Zhang *et al.* 2010). Conventional CTA plays a limited role in the evaluation of cerebrovascular function near the base of the skull because of difficulties in separating vessels from bone structures (Zhang *et al.* 2010), but it is still used in some CT scanners.

2.3 Radiophotoluminescence (RPL) dosimetry

2.3.1 Development of RPLD material

In medical radiation applications, different radiation types and energies set particular demands for dosimetry. The large energy range requires low energy dependence from the dosemeter material. For diagnostic dosimetry, a dosimeter must be capable of measuring very low radiation doses.

In the early 1960s, fluoroglass dosimeter (FD) material was further developed. The glass consisted of phosphorus, aluminum, lithium, silver, magnesium, and barium oxides. The property of the early lithium borate glasses was their naturally low energy dependence, but there were also handling problems due to the composition of the material (Perry 1987). The kinetics of the material is dependent on the element compounds; for example, after irradiation, radiation energy accumulated more rapidly in the basic element of $LiPO_3$ than in $Al(PO_3)_3$ material (Perry 1987). It was also observed that reducing the content of the alkali metals decreased the sensitivity of RPL dosimeters due to low Ag^+ ion mobility in

glasses (Dmitryuk *et al.* 1996). The concentration of silver was much higher in early glasses than in more recently used materials (Perry 1987). The concentration of silver and sodium in the basic element material is responsible for the background luminescence called predose in the material (Perry 1987, Fan *et al.* 2013).

Predose is caused by fluorescence intensity emitted by an unirradiated glass material. The predose is not a problem in high dose measurements, such as radiation therapy doses, but it plays an important role in measuring radiation doses less than 100 μGy (Perry 1987). Sensitivity, predose, and energy dependence were subsequently improved with advantages to personnel monitoring. The improvements were necessary because the early glasses were not suitable for low-dose measurements (Perry 1987). The more recently used glass material was improved by replacing lithium with sodium (Fan *et al.* 2013), and the silver concentration in the material was reduced (Perry 1987, Hsu *et al.* 2010a). Also the element composition of the glass material affects the capability of UV spectrum to penetrate the glass material. Using reduced silver and aluminum concentrations improved the excitation of luminescent centers by UV laser (Hsu *et al.* 2010a, Hsu *et al.* 2010b). The recently used glass material weight composition is Na (11.0%), P (31.55%), O (51.16%), Al (6.12%) and Ag (0.17%) with a density of 2.61 g/cm^3 (Perry 1987, Hsu *et al.* 2006, Mizuno *et al.* 2008, Rah *et al.* 2009b, Kadoya *et al.* 2012).

2.3.2 Radiophotoluminescence phenomena

Radiophotoluminescence (RPL) dosimetry is based on luminescence phenomena. Luminescence is divided into two phenomena; phosphorescence and fluorescence. Phosphorescence decay to ground state is considerably longer than that of the fluorescence. The luminescence process in RPL is fluorescence. Fluorescence is defined as luminescence that persists only for as long as the exciting radiation is present. (Perry 1987).

In solid dosimeter material, where the atoms are close together, energy bands are formed if the outer shells of electrons lie close enough to each other. The highest energy level is the conduction band, where the electrons have sufficient energy to move through the crystalline lattice. The next energy band is the valence band which contains the valence electrons. In pure materials, there is a forbidden energy band where electrons cannot exist (Dendy & Heaton 1999). If the crystal contains impurities, additional energy levels or electron traps are

formed in the forbidden energy band, and luminescence phenomena are possible (Perry 1987). In solid state dosimeters, impurities are added to produce the ideal number and types of traps (Dendy & Heaton 1999). When the luminescence material is irradiated, the electron-hole pairs are formed (Figure 4 A). The electrons (e^-) lift up into the conduction band where some of them are immediately trapped by positively charged silver ions and holes (h^+) trapped by negatively charged phosphate ions. Another luminescence center is formed by hole-phosphate compounds towards the positively charged silver ions (Perry 1987) (Figure 4 B). The forbidden energy level close to the conduction band is called electron trap, and the one close to the valence band is called hole-trap (Figure 4 C).

The absorbed energy in the material is directly proportional to the number of traps formed (Dendy & Heaton 1999). The characteristic of the RPL glass dosimeter is that unique metastable absorption and emission bands are created by ionization radiation permitting the quantification of the dose delivered to the glass (Perry 1987). After excitation of the luminescence centers by pulse UV laser with a specific wavelength, a specific fluorescence emission spectrum is observed (Figure 4 C). The amount of the fluorescence emission is proportional to the dose delivered to the dosimeter (Perry 1987). The dosimeters can be reused after an annealing procedure. Thirty minutes annealing at 400°C will empty the dose in the dosimeter by releasing electrons from the traps back to the valence band (Lee *et al.* 2009, Knezevic *et al.* 2013) (Figure 4 D). The annealing time is dependent on the dose level in the dosimeter (Perry 1987, Rah *et al.* 2009a).

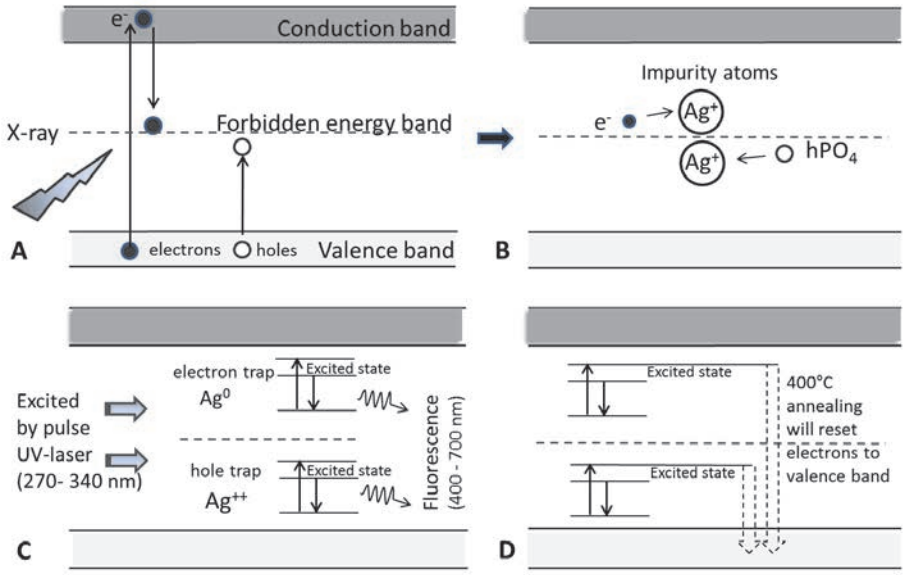

Fig. 4. A and B) Schematic representation of creation of stable luminescent centers (Ag^0, Ag^{++}) by X-ray, C) fluorescence emission after UV excitation and D) annealing in 400°C to empty dosimeters (modified from Lee *et al.* 2009 and Huang & Hsu 2011).

2.3.3 Luminescent centers in RPLD material

RPLD material consists of a glass substrate incorporating ions of silver (Ag^+) and phosphate (PO_4^{3-}), (Figure 4 and 5). The location of these ions represents defects in the lattice of the dosimeter material (Perry 1987). Irradiation releases electrons in the dosimeter material; as a result, there are electron-hole pairs which are caught by Ag^+ ion and PO_4^{3-} ion, creating stable luminescent centers (Ag^0, Ag^{++}) (Figure 5), which are defined for the electron trap as

$$Ag^+ + e^- = Ag^0 \quad (28)$$

and for the hole trap as

$$Ag^+ + hPO_4 = Ag^{++} \quad (29)$$

(Perry 1987, Miyamoto *et al.* 2010).

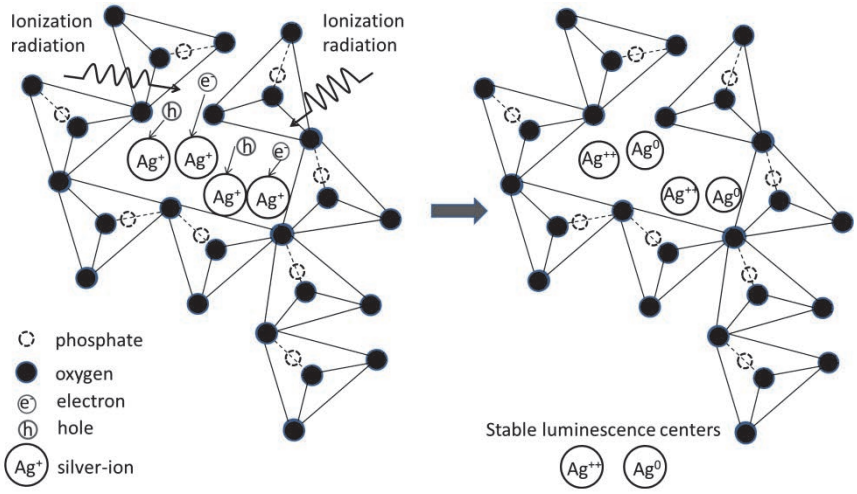

Fig. 5. RPLD material consists of a glass substrate incorporating ions of silver (Ag^{+}) and phosphate (PO_4^{3-}). Schematic representation of stable luminescent centers (Ag^{++}, Ag^{0}) which are generated in silver glass by ionization radiation (modified from Huang & Hsu 2011).

The traps are stable in the sense that the energy required to remove the electron or hole from the trap to the conduction or valence band must be much larger than the binding energy of the electron in the trap. The negligible fading in a dose absorbed into the RPLD material is caused by the metastable luminescent centers of Ag^{0} and Ag^{++} ion (Piesch *et al.* 1993, Lee *et al.* 2009, Yamamoto *et al.* 2011, Miyamoto *et al.* 2011). The electrons move slowly to the traps and dose fading is minimal. During the irradiation of the silver-activated phosphate glass, luminescent centers begin to form. However, the formation of these centers does not appear immediately, because some of the electrons are caught in ineffective traps which do not produce luminescence. After a ten- and hundred-day follow-up study at room temperature, 90% and 99% of the total dose of the dosimeter is reached, respectively. This phenomenon is known as the build-up effect and requires a stabilization treatment by heating in 70°C or 100°C (Hsu *et al.* 2006, Yamamoto *et al.* 2011, Knezevic *et al.* 2013). The electrons diffuse faster than holes in the glass material, and the accumulation speed of Ag^{0} is thus higher than that of Ag^{++}. This build-up effect is stabilized by heating. The heating treatment causes faster accumulation of Ag^{++} in the irradiated dosimeter and is responsible for the creation of the main RPL centers (Yamamoto *et al.* 2011). After the heating procedure, the luminescent centers remain relatively constant in room

temperature over an extended period, and dosimeters permit repeated measurements free from the fading effect (Perry 1987, Hsu *et al.* 2006, Lee *et al.* 2009).

Stable luminescent centers are able to absorb and release energy (Perry 1987); this is used as the principle in the dosimeter readout system. When the luminescent centers are irradiated by pulsed ultraviolet laser (270–340 nm), electrons are excited into a higher energy state. The centers return to a stable energy level by emitting light (420–700 nm) known as fluorescence (Miyamoto *et al.* 2010). The fluorescence is measured with a photomultiplier system, and the amount of fluorescence is directly proportional to the dose absorbed into the dosimeter (Lee *et al.* 2009, Yamamoto *et al.* 2011).

The higher exciting wavelength is used for 620 nm emission due to the better low-dose response in the reader (Perry 1987). Currently, the excitation of 337.1 nm pulsed ultraviolet laser beam is used in the low dose readout system producing an orange emission band of 600–700 nm (Dmitryuk *et al.* 1996, Hsu *et al.* 2007, Lee *et al.* 2009, Knezevic *et al.* 2013).

2.3.4 Energy dependence and compensation

In radiology, relatively low energies between 10 keV and 140 keV are used. At these energies, the relative response of the dosimeter is high because of the strong dependence between the effective atomic number and the photoelectric effect (Perry 1987). A minimal energy dependence or deviation of response with changing energy is required from the dosimeter. This is particularly required in the dose measurement of the continuous spectrum. The relative energy response of the dosimeter material can be expressed as the ratio between peak and minimum response energy (Perry 1987). Usually, the minimum response energy is defined at 1 MeV or at the ^{60}Co energy of 1.33 MeV. The peak response is the highest dose determined with the energy spectrum (Perry 1987). The peak response is determined in RPLD glass material at about 30–45 keV (Perry 1987, Hsu *et al.* 2007). The energy dependence of the dosimeter is defined as the ratio of the absorbed energy at two reference points on the energy axis.

The mass energy absorption coefficient of the RPLD is higher than that of soft tissue and almost similar to bone in the energy region used in radiology (Perry 1987). The mass energy absorption coefficient of RPLD is calculated from Equation 30 (Figure 6 A). If the mass energy absorption coefficients for mixtures and compounds are assumed to be homogenous, they are calculated as

$$\frac{\mu_{en}}{\rho} = \sum_i W_i \left(\frac{\mu_{en}}{\rho}\right)_i \quad (30)$$

where W_i is the fraction by weight of the ith atomic constituent, and the $(\mu_{en}/\rho)_i$ values are from the NIST Standard Reference Database, 126 NISTIR 5632. (Hubbell & Seltzer 1996).

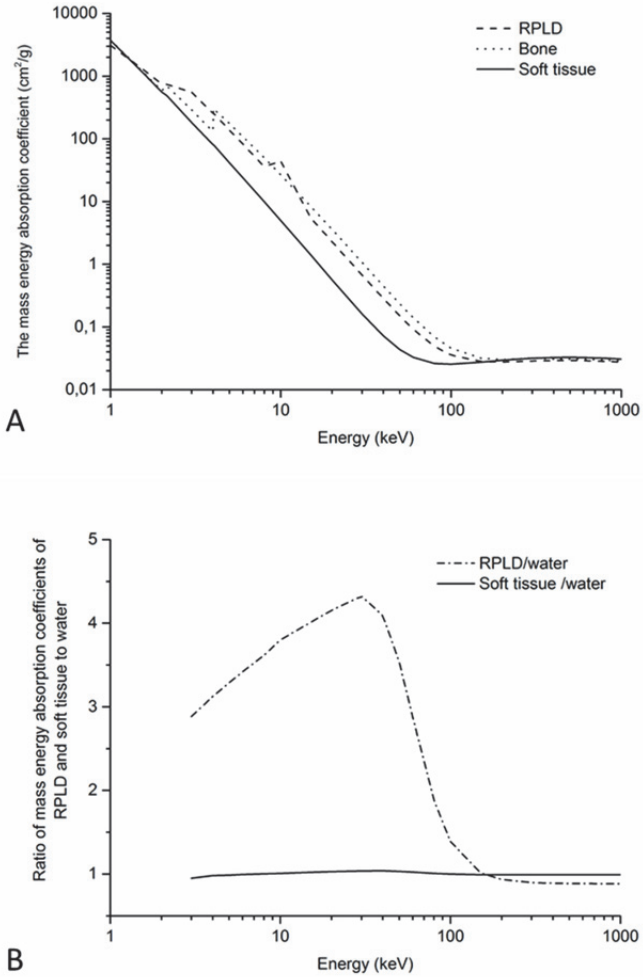

Fig. 6. A) The mass energy absorption coefficients of RPLD, bone and soft tissue and B) RPLD and soft tissue to water. Produced from NIST Standard Reference Database, 126 NISTIR 5632 (Hubbell & Seltzer 1996).

Although previously used dosimeter materials have been improved, they still have a higher effective atomic number (Z_{eff} =12.0) than soft tissue (Z_{eff} =7.4). The interaction between radiation and RPLD material occurs through the photoelectric effect (Figure 7). The ratio of the mass energy absorption coefficient is determined as being up to four-fold between RPLD material and water (Mizuno *et al.* 2008) and between RPLD material and air (Kadoya *et al.* 2012).

The material of the dosimeter used in radiation dose measurements, such as absorbed dose determination of organs, should be close to the properties of the tissue when determining the radiation doses for patients. The over-response of the dosimeter material is compensated by using a filter, or the use of calibration factors is recommended at low X-ray energies (Perry 1987, Hsu *et al.* 2007). The simplest method is to cover the surface of the dosimeter to be irradiated with a single metal filter. When choosing a filter material, the position of the K-absorption edge of the material must be considered. Previously, several metals have been tested as filters in high atomic number glasses and at high energies (Perry 1987). Lead, tantalum, copper and cadmium produced a flat response only in a very narrow energy range; these metals were considered unsuitable for low energies due to too high absorption efficiency of low photons (Perry 1987). Furthermore, it was observed that more effective compensation could be achieved by partial filtration or by making holes in the filter material. For example, 85% surface shielding was used (Perry 1987). Improved flat response was observed when using this method for low Z glass. For low energy X-ray, aluminum and tin were tested. A tin filter was observed to be better because of a flat response (Perry 1987). A tin filter has a K edge of 29.1 keV, and the absorption of 25–40 keV photons is efficient at X-ray energies (Figure 7). The K edge is defined as a discontinuity in the absorption coefficient at an energy level corresponding to the binding energy of K-shell electrons. The mass absorption coefficient increases rapidly when photon energy overcomes the binding energy of the K-shell electron (Dendy &Heaton 1999).

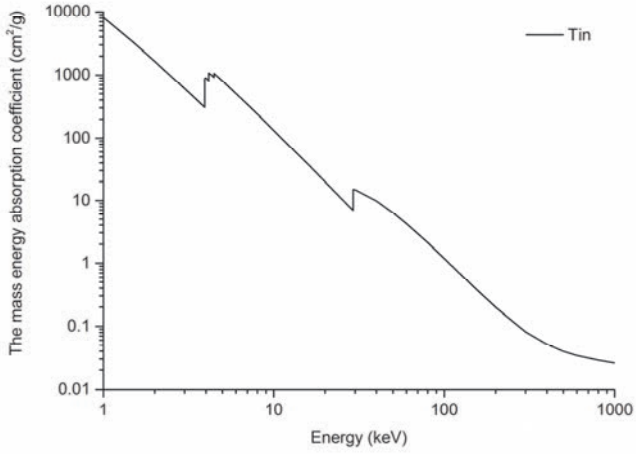

Fig. 7. The mass energy absorption coefficient of tin. Produced from NIST Standard Reference Database, 126 NISTIR 5632 (Hubbell & Seltzer 1996).

The energy dependence between 25 keV and 1.3 MeV energies was reported to vary from ±10% to ± 30% using an energy compensation filter made of tin (Perry 1987, Piesch & Burgkhardt 1994, Hsu *et al.* 2006).

2.3.5 Angular dependence

The variation in response of a dosimeter with the angle of incidence of radiation is known as the directional, or angular, dependence of the dosimeter. Dosimeters usually exhibit angular dependence due to their constructional details, physical size, and the energy of the incident radiation (Perry 1987). Angular dependence is important in certain applications; e.g., in *in vivo* dosimetry, in phantom measurements used in determination of absorbed and effective dose, and in entrance skin dose measurements (Perry 1987). Especially, angular dependence must be taken into consideration when using a dosimeter covered by a filter. In actual measurements, dosimeters should be used in the same geometry as they are calibrated in (Perry 1987, Kadoya *et al.* 2012, Kato *et al.* 2013). The angular dependence of the RPLD has been previously investigated for dosimeters without a tin filter. The angular dependence was reported to be from 1% to 5% in

horizontal direction and from 4% up to 16% in vertical direction of the cylinder-shaped dosimeter without a tin filter (Araki *et al.* 2003, Araki *et al.* 2004, Hsu *et al.* 2007, Rah *et al.* 2009a, Rah *et al.* 2009b). The angular dependence has particular significance in dosimetric applications in patients or phantoms where the direction of the photon beam is variable, for example in fluoroscopy and computed tomography.

2.3.6 Dose measurement range

The radiophotoluminescence glass dosimeter material has a linear relationship between the fluorescence intensity and the dose caused by ionizing radiation (Perry 1987, Hsu *et al.* 2006, Hsu *et al.* 2007, Rah *et al.* 2009a). The low dose limit is dependent on the predose, which is meant to quantify the level of background effects that are inherent within the glass. The challenge is to separate the RPL emission band from the unwanted predose luminescence. The predose is a function of both glass and reader technique (Perry 1987).

In the 1990s, an automatic readout system was created, which uses pulsed ultraviolet (UV) laser excitation and pre-dose suppression (Hsu *et al.* 2007). After the development of the measurement technique of a pulsed UV laser, the detection of small doses in the 10–30 μGy range was possible with sufficient accuracy (Perry 1987, Piesch *et al.* 1993). The technique is based on electronic discrimination of signals from the predose and the actual dose due to their different fluorescence decay times (Perry 1987, Piesch *et al.* 1993, Piesch *et al.* 1994). After pulsed UV laser (337.1 nm) excitation, electrons return to a stable energy level in the luminescence center by emitting fluorescence (620 nm). The fluorescence emission is imaged by a lens onto a photomultiplier (PM). A timing circuit triggers the main RPL emission, measuring time at 2–7 μs (t_1) and long decay predose at 40–45 μs (t_2) (Figure 8). RPL emission (M) is calculated as

$$M = \int_{t_1} I(t) - fps \int_{t_2} I(t)\, dt \tag{31}$$

where $I(t)$ is fluorescence intensity at time t and fps is a correction factor for the predose in the glass itself (ATGC 2004), (Figure 8).

The dose is reported to be linear up to at least 30 Gy, becoming sublinear at higher doses (Perry 1987). The point where sublinearity occur depends on the glass dimensions and material, the reader technique, and the spectral region in which the fluorescence is measured (Perry 1987, Hsu *et al.* 2007).

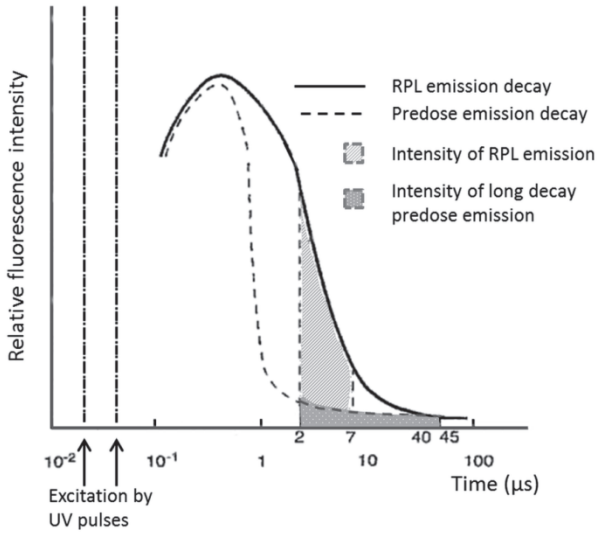

Fig. 8. Schematic representation of pulsed laser excitation, predose and RPL emission and their different fluorescence decay times (modified from Piesch *et al.* 1994 and Instruction Manual, ATGC 2004).

2.3.7 Accuracy and errors

Calibrating the dosimeters is recommended to be carried out against a suitable ionization chamber or dosimeter whose calibration is traceable to a standard laboratory (Zoetelief *et al.* 2000). Verifying the dosimeter must be done to determine the energy, angular response, dose response linearity, fading effect of the dosimeter, and detection threshold. Dosimeters are usually calibrated in terms of air kerma or entrance surface dose (ESD) (Zoetelief *et al.* 2000).

With regard to overall system performance, the effect of errors is greatest at the lowest doses (Perry 1987). The contribution from different sources of errors must be taken into consideration in order to characterize the system in terms of reliability or reproducibility. The equation for estimating the dose (D) can be formulated as

$$D = ((D_{meas} - D_{instr}) - D_{BG})K_{cal}K_E K_F \quad (32)$$

where D_{meas} is dosimeter dose measured from each irradiated dosimeter, D_{instr} is an individual dose from a freshly annealed dosimeter, D_{BG} is dose of background

radiation from a control dosimeter, K_{cal} is dosimeter dose response to doses from a reference radiation source, and K_E is an energy correction factor, defined as $K_E^{-1} = R_E K_{cal}$, where R_E is the dosimeter response for photons of energy E, while K_F is a fading correction factor (Zoetelief *et al.* 2000).

The error of measurement is defined as the difference between a measured value of a quantity and a 'true value' of that quantity. The errors due to operator are estimated to be 2–4% with handling of the RPLD (Perry 1987). All errors which are caused by glass material, reader, or operator must be minimized by verifying precise dose determination (Perry 1987). The disadvantage of dosimeter handling is that the glass must move from the plastic holder during the heating and read-out procedure. In this process, the glass may get foreign material onto the surface, and this may cause extra fluorescence and raise the predose (Perry 1987). For low-dose measurements, the individual dosimeter doses (D_{instr}) have to be measured before irradiation. D_{instr} must be subtracted from the individual dosimeter dose (D_{meas}) to minimize the predose effect. During the irradiation and handling of RPLD, encapsulation protects the glass from dirt and grease (Perry 1987). The dose response at energy ranges below 25 keV is reported to decrease due to the thin plastic holder (Kadoya *et al.* 2012). Dosimeters should be encapsulated in the same way during calibration and use (Zoetelief *et al.* 2000).

The glass dosimeter is made of cooled liquids of homogenous glass substrate and is responsible for good batch uniformity. The method ensures minimal variation in the glass compositions. TLD is made of crystal and its batch uniformity is about 10% (Perry 1987, Piesch *et al.* 1990), compared to ±1.0–±1.5% in RPLD (Perry 1987, Piesch *et al.* 1990, Hsu *et al.* 2007). Each single glass detector does not need individual calibration.

Build-up may cause significant uncertainties if the dosimeter heating treatment is not used after the irradiation (Knezevic *et al.* 2013). The heating temperature must be in relation to the calibration of the dosimeter. Fading effect was reported to be very low, less than 1%, and using the fading correction factor is not necessary (Hsu *et al.* 2006).

The overall stability of the reader is responsible for the reproducibility of the measurement itself. Repeated measurement on the same glass without moving the glass between measurements is reported as being 1–1.5% (Perry 1987), and reproducibility is improved to a CV of 0.4–0.55% after ten repetitions on average with a modern reader (Hsu et. al 2006, Knezevic *et al.* 2013).

3 Purpose of the study

The aim of this thesis was to assess the applicability of RPL dosimetry for dose determination in radiology. The specific aims of this study were:

1. to determine the applicability of RPLD for measuring radiation doses in air and on the surface of the phantom by systematically assessing various properties of the RPLD;
2. to determine the absorbed dose in vaginal fornix for pregnant women undergoing fluoroscopy imaging during prophylactic catheterization before UAE treatment by using RPLD;
3. to compare the effective doses of CTA and DSA for a typical four-vessel angiography of the cerebral and cervicocerebral area, by using the same dose determination technique with RPLDs in an anthropomorphic phantom.

4 Materials and Methods

4.1 Materials

This study was carried out at the Department of Diagnostic Radiology of Oulu University Hospital. The various properties of the radiophotoluminescense dosimeters (RPLD) were determined for verifying the applicability of the dosimeters for the radiation exposure evaluation in the energy ranges used in radiology (Study I). The verification of the dosimeters was carried out in air and on the surface of a phantom. Also RPLD was applied for the estimation of absorbed and effective dose. The absorbed dose measurement was carried out through vaginal measurements in pregnant women undergoing fluoroscopy imaging during prophylactic catheterization before uterine artery embolization (UAE) (Study II). To evaluate the radiation exposure of two different angiography imaging methods, effective doses were determined for the DSA and CTA of the cerebral and cervicocerebral vessels (Study III).

4.1.1 Phantoms

PMMA phantom

The entrance surface dose (ESD) was examined by positioning the dosimeters on the surface of a PMMA (polymethylmethacrylate) phantom 10 cm thick and measuring 20 cm x 20 cm, with 1.190 g/cm^3 density, with a relative composition of C (60.0%), O (32.0%) and H (8.1%) to determine the energy dependence of RPLD in Study I.

Anthropomorphic phantom

The simulation of the absorbed and effective dose of the angiography procedures in Study III was performed by using an anthropomorphic phantom (Alderson-Rando Phantom; Alderson Research Laboratories, Long Island City, New York) consisting of a human skeleton and simulated lung tissue with similar attenuation as that of lung, encased in tissue-equivalent plastic material. An anthropomorphic phantom is molded to the shape of the human body and divided into transverse sections of 2.5 cm thickness, including holes in the z-direction to place the

dosimeters perpendicularly to the photon beam. The phantom consists of 36 separate sections (Scalzetti *et al.* 2008) (Figure 9 A and C). The phantom has simulated breast tissue that was custom-made of paraffin, which has similar absorption as fat. Breasts were molded directly onto the anthropomorphic phantom surface to ensure fit and to prevent air gap between phantom and breast. 3 mm diameter holes were bored for placing the dosimeters along the z-direction inside the simulated breasts. RPL dosimeters were located at the depth of 2 cm from the surface of the breast. The breasts were 4.5 cm thick. The volume of the right breast was 500 ±10 ml and the left breast volume was 485±10 ml (Figure 9 B).

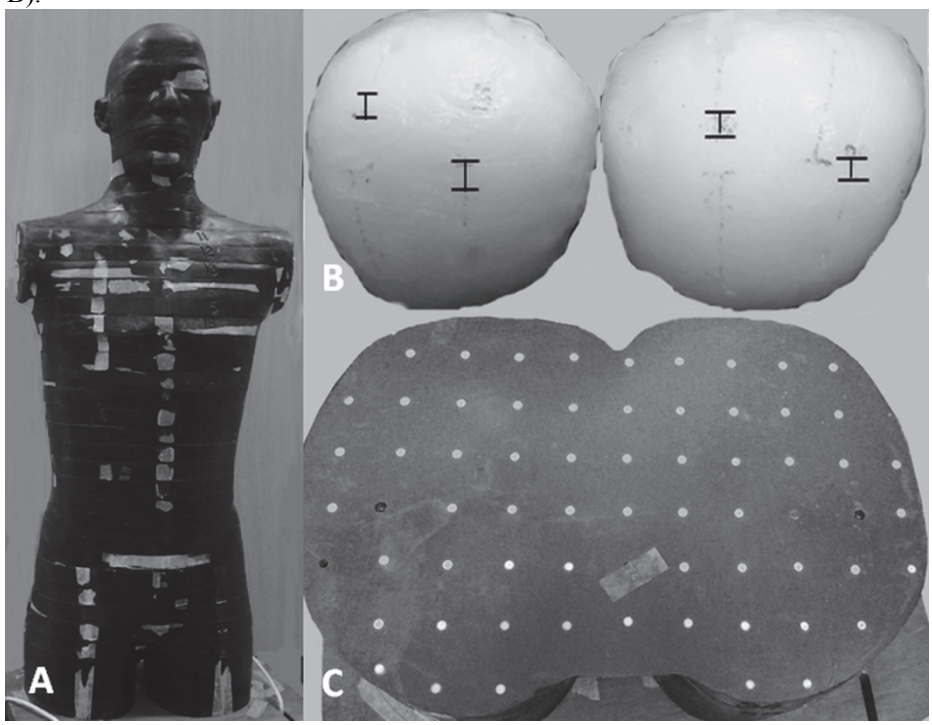

Fig. 9. A) Anthropomorphic phantom and B) simulated custom made breasts with marks for RPL dosimeters locationing along the z-direction at the depth of 2 cm C) a cross-section of the phantom used in the current thesis.

Effective dose measurement requires average organ dose calculation, and the spatial extent of organs is needed. Any given location in the phantom was identified by means of a three-dimensional Cartesian coordinate system to

facilitate the implanting of the dosimeter in the phantom (Scalzetti *et al.* 2008). These landmarks were used in the current study.

4.1.2 Patients

In Study II, the absorbed dose measurement was carried out through vaginal measurements comprising seven women who underwent prophylactic catheterization before an elective cesarean section for prospective arterial embolization at Oulu University Hospital during years 2008–2011. The study was approved by the local ethics committee. All patients were selected according to medical need, having a high risk of postpartum hemorrhage, and catheterization was done in order to avoid excessive bleeding. The absorbed doses were determined in vaginal fornix by four numbered X-ray-positive RPL dosimeters. Magnetic resonance images (MRI) were utilized for the measurement of the dimensions of the mother and fetus (Table 2).

Table 2. Dimensions of seven pregnant women.

Patient	No.1	No.2	No.3	No.4	No.5	No.6	No.7
Diameter (cm)[1]	23	28	29	26	29	28	28
Distance (cm)[2]	10	11	14	10	11	11	11

[1]Diameter of the patient (cm), [2]Distance from mother's back surface to fetus (cm)

4.1.3 Equipment

RPLD read-out device

The dose determination was performed using an automatic RPLD read-out system (Dose Ace FGD-1000, Asahi Techno Glass Corporation, Chiba, Japan) (Figure 10).

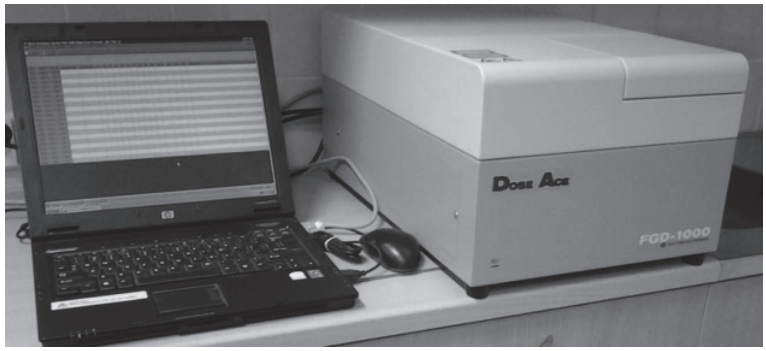

Fig. 10. Automatic RPLD read-out device (FDG-1000).

The equipment utilizes a pulsed UV laser (N2 gas laser) measurement technique (Figure 11). The UV laser beam is collimated by a convex lens using a UV pass filter of 337.1 nm wavelength. The filtered UV light is guided through a diaphragm to a mirror where it is split into two beams, one for a sample glass and the other for a reference glass. After a short UV excitation, a fluorescence emission is observed. The fluorescence emission is imaged by a lens using a UV cut-off filter. An interference filter is used for reducing interference between UV scattering and fluorescence emission to prevent fluorescence elimination. A photomultiplier is used for detecting the fluorescence emission of the sample. The error caused by the variation of UV laser pulse is corrected with the help of the reference glass emission detected by a photodiode. The signals are pre-amplified and digitized for further calculation on computer. A timing circuit triggers the main RPL and the long decay predose emission measuring time (Figure 8). A trigger circuit is used for timing the frequency of laser pulses, 20 pulses per second in the current work. A calibration glass inside the reader is used for the automatic internal calibration of each reading cycle. The calibration glass has been set against the standard calibration glass (type GDS-352A) to 6 mGy dose (ATGC 2004).

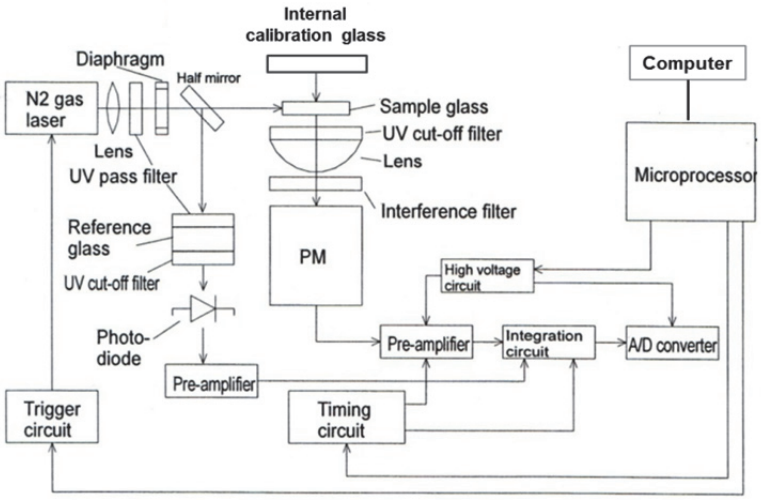

Fig. 11. Schematic representation of FGD-1000 read-out system (modified from Instruction Manual, ATGC 2004).

Calibration of the RPLD read-out device

The read-out device was calibrated according to the manufacturer's instructions with pre-radiated standard calibration glass type GDS-352A (Asahi Techno Glass Corporation, Chiba, Japan) in the 10 μGy–10 Gy dose range. Standard calibration glass was irradiated by the manufacturer using ^{137}Cs gamma radiation (6 mGy in air). The RPLD dose (D_{meas}) is expressed as

$$D_{meas} = \frac{M}{REF} N \tag{33}$$

where *REF* is the dose measured from reference glass and *M* is RPL emission detected from sample glass (see Equation 32). The calibration factor (*N*) is expressed as

$$N = nc \frac{Dst}{M_{st}} \tag{34}$$

where a reader correction factor *nc* is used for energy correction purposes. In the current study, *nc* was 1.000 for X-ray energies in the energy ranges used in

radiology. D_{st} is the dose value of standard glass including irradiated dose (6 mGy) and inherent predose of standard glass (ATGC 2004). Natural background dose per month was fed into the system at first calibration of the device and is automatically subtracted by the system from the standard glass dose (D_{st}). To ensure the correct calibration level in dose measurements, irradiated sample dosimeters were heated for 30 min at 70ºC (ATGC 2004). The dosimeters were preheated and read out immediately after irradiation.

RPL dosimeter

In this thesis, glass dosimeter type GD-352M (Asahi Techno Glass Corporation, Chiba, Japan) was used in dose detection with an energy compensation filter made of tin. The dimensions of the plastic capsule of the dosimeter were 3 mm x 12 mm (Figure 12).

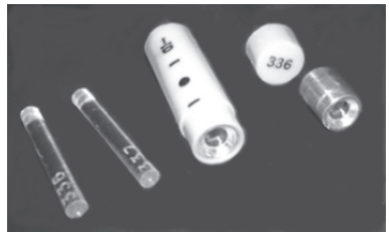

Fig. 12. RPL dosimeters made of glass with a plastic capsule and tin filter.

Reference measurements

To verify the calibration and to evaluate the properties of the RPLD, reference measurements were made with a Radcal dosimeter (model 9015, Radcal Corporation, Monrovia, CA, USA) with an ionization chamber (type 10;5–6, General Purpose, Beam Chamber). The ionization chamber has an energy dependence within ±5% in the 30 keV and 1.33 MeV energy range. In the present study, reproducibility was tested before use and it amounted to 1.8% after three repeated measurements.

Imaging equipment

The properties of dosimeters were examined using a conventional radiography system (Siemens Axiom Aristos FX, Plus, Erlangen, Germany) and a

mammography system (GE-Senografe Essential, General Electric Company, Waukesha, WI, USA) for energies less than 30 keV (Study I).

Prophylactic catheterization and embolization was done using angiography imaging equipment with a flat panel detector (GE Healthcare, Innova 4100 IQ, Buc, France) (Study II).

Biplane angiography equipment with image intensifier detectors (Integris Allura 12 and 15 biplane; Philips Healthcare, Best, the Netherlands) was used in the simulation of DSA, while CTA was performed by using a 64-row MDCT scanner (Somatom Sensation 64; Siemens, Erlangen, Germany) (Study III).

The quality control tests for the imaging equipment were carried out once a year including DAP meter and DLP display verifications.

4.2 Methods

4.2.1 Properties of RPLD for dose measurements in radiology

The energy and angular dependence, the linearity of the dose response, the fading effect, and the measurement accuracy at radiologic photon energies and doses were studied. The properties of dosimeters were examined using a conventional radiography system with a 0.1 mm Cu filter for energies higher than 40 keV. The focus to dosimeters distance was 100 cm and the field size was collimated at 10 cm x 10 cm. A mammography system with a rhodium filter was used for energies less than 30 keV. The field size was collimated at 10 cm x 10 cm and the focus to dosimeter distance was 56 cm. The irradiation was done in air in all cases expect for the entrance surface dose measurements for the energy dependence using a PMMA phantom block.

4.2.2 Absorbed dose determination in vaginal fornix of the pregnant women during the prophylactic catheterization

The prophylactic catheterization before the uterine artery embolization (UAE) was carried out using angiography imaging equipment with a flat panel detector. The X-ray tube was placed under the table. The angle of the X-ray beam varied depending on the patient's position on the table. During the treatment, pulsed fluoroscopy with the lowest possible pulse rate for our equipment and the last image hold (LIH) technique without angiography exposures were used. The

parameters for the fluoroscopy procedure were as follows: fixed 92 kVp tube voltages, pulse rate of 15 pulses per second, filtration of 3 mm Al and 0.3 mm Cu. The effective energy was 50–60 keV (Figure 13).

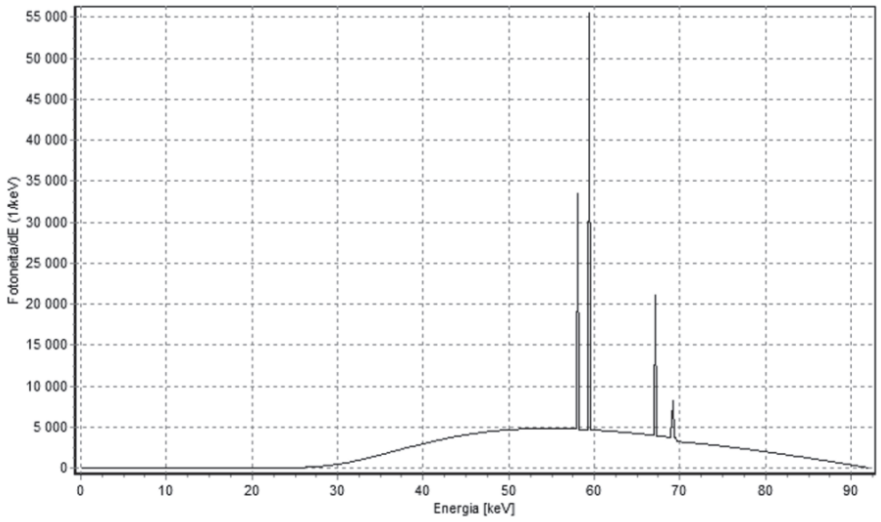

Fig. 13. The used energy spectrum in fluoroscopy protocol during the cathetrization of the pregnant women was generated by the program STUK-TR 3 (Tapiovaara & Tapiovaara 2008).

The tube current varied depending on the patient's diameter by using automatic brightness control (ABC). The field of view (FOV), source to image-detector distance (SID), focus to skin distance (FSD), and collimation were adjusted by the radiologist. The prophylactic catheterization was performed under fluoroscopy guidance using a tight collimation. After bilateral transfemoral punctures, the internal iliac arteries were catheterized selectively, and long introducer sheaths were introduced into the proximal parts of the internal iliac arteries. Then, an angiography catheter was advanced into the anterior trunks of both internal iliac arteries and catheters were fixed. The correct position of the catheter was checked by the radiologist using a small bolus of contrast medium and low-dose pulsed fluoroscopy imaging. The radiation exposure during the catheterization was mostly focused on the anterior trunks of both internal iliac arteries where the catheters were fixed (Figure 14).

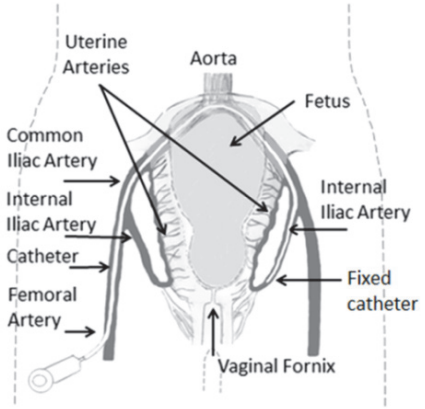

Fig. 14. Schematic representation of the prophylactic catheterization before uterine arteries embolization of the pregnant woman.

During the catheterization, the radiation exposure of the treatment was measured by RPL dosimeters. Four numbered X-ray-positive RPL dosimeters were stored in Eppendorf tubes in a plastic bag (Figure 15 A). The plastic bag was put in a sterile glove to place within the vagina to estimate the absorbed dose in vaginal fornix (Figure 15 B) (Study II). The elective cesarean section was performed and, at the same time, the dosimeters were taken out of the vagina and immediately measured. After the delivery of the infant, the embolization of the uterine arteries was done.

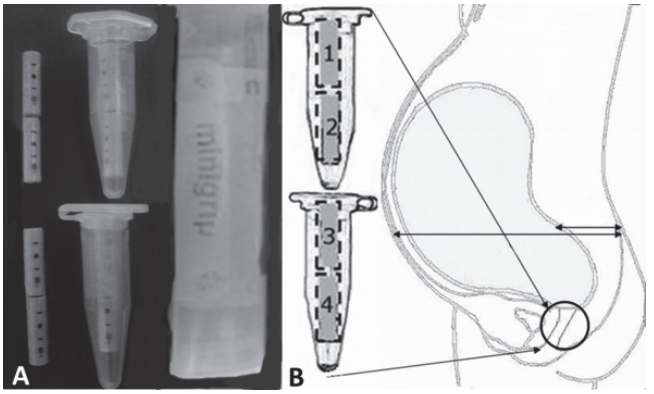

Fig. 15. A) RPL dosimeters were stored in Eppendorf tubes in a plastic bag and B) placed within the vagina (published by permission of Springer).

4.2.3 Phantom measurements of DSA and CTA for a typical angiography of the cerebral and the cervicocerebral vessels

Imaging equipment and protocols

CTA was performed by using a 64-row MDCT scanner (Figure 16 A). The cerebral CTA examination was based on the manufacturer's protocol. The tube voltage was 100 kVp and the effective tube current time product was 148 mAs in the cervical examination using the tube current modulation technique and projection-based real-time tube current modulation. The tube voltage was 120 kVp and the constant tube current time product was 160 mAs in the cervicocerebral examination.

The simulation of DSA examinations for cerebral and cervicocerebral vessels was simulated by a radiologist using biplane angiography equipment and protocols in clinical use at Oulu University Hospital (Figure 16 B). Automatic exposure control and filtration of 2.9 mm AL and 0.1 mm Cu was used in the DSA examination. Seven angiography imaging series were included in the cerebral angiography protocol; the total number of frames was 224. Eleven angiography imaging series were included in cervicocerebral angiography and the total number of frames was 275. One three-dimensional rotation angiography (3DRA) series with 100 frames was included in both imaging protocols. The fluoroscopy time was 5 minutes in both protocols. The tube voltage varied between 75–90 kVp depending on the used plane. The tube current time product was between 14 and 114 mAs in the anterior-posterior plane, and between 15 and 27 mAs in the lateral plane, depending on the anatomic location of the imaged object. With both modalities, the protocols were optimized by a neuroradiologist and physicist and are in routine clinical use at our institution. The detailed protocols are described in Study III.

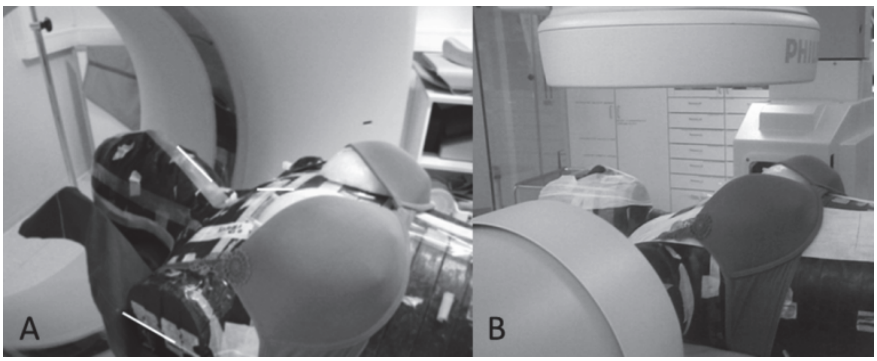

Fig. 16. A) A 64-row MDCT scanner for CTA and B) a biplane angiography equipment with image intensifier detectors for DSA was used; the phantom was positioned by laser light in CTA and by fluoroscopy in DSA examination.

Absorbed and effective dose determination

The absorbed and effective doses were determined for the diagnostically optimized protocols of CTA and DSA for cerebral (intracranial) and cervicocerebral (from the aortic arch to vertex) arteries (Figure 17). The imaging began at phantom level 5 for the cerebral vessels and at phantom level 15 for the cervicocerebral vessels (Figure 18).

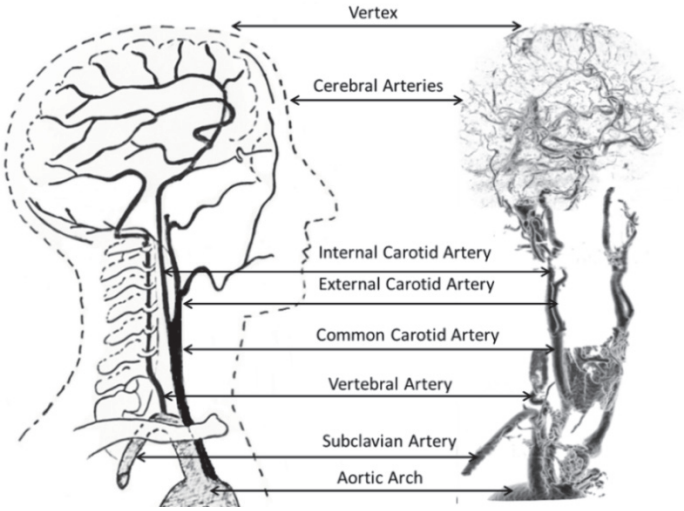

Fig. 17. Schematic representation of the cerebral and cervicocerebral vessels.

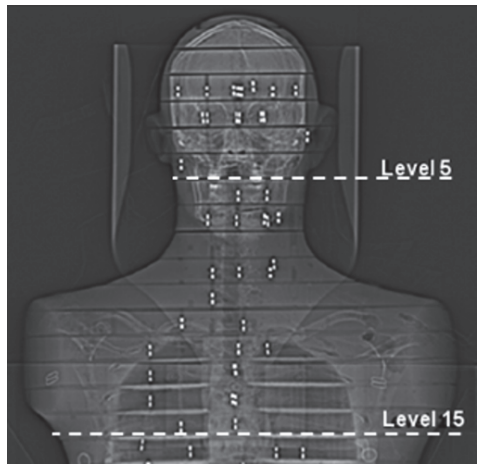

Fig. 18. Scout image of anthropomorphic phantom with 2.5 cm interslice.

All organs within the primary beam were covered by the dosimeters. The dose measurements were also performed for organs outside the primary beam because these areas are exposed to scattered radiation. Depending on the organ volume, 1–9 dosimeters were placed in each organ in the same locations with both imaging methods. Also, depending on the acquisition protocol, the phantom was equipped with at least 69 RPLDs. The detailed locations of the dosimeters in the anthropomorphic phantom are presented in Study III.

Three simulation runs were performed to improve the accuracy of the measurement for both DSA protocols. CTA was simulated 3 times for cerebral vessels and once for cervicocerebral vessels. Three repeated acquisitions were used in CTA for each simulation run. In addition, the phantom was positioned using laser light to ensure the same position between the CTA simulation runs.

The equivalent doses (H_T) were calculated using Equation 26. The average absorbed dose of tissue ($D_{Ti,}$) was multiplied by irradiated fraction (f_i) of *i*th tissue *T*. The fractions are shown in Table 3. The equivalent dose to active bone marrow was calculated by using the sum of the individual weighted doses based on the distribution of active bone marrow throughout the adult body (Cristy & Eckerman 1987) (Table 3). Bone surface dose was calculated by multiplying active bone marrow dose with 4.64 (Ludlow *et al.* 2006). The dose to lymphatic nodes was calculated by using the sum of the individual weighted mean absorbed doses of the surrounding organs (Tapiovaara & Siiskonen 2008) (Table 3). Extra thoracic airways, muscles and skin dose were determined by calculating the mean dose of

detection points (Tapiovaara & Siiskonen 2008, Ludlow *et al.* 2006) (Table 3). The equivalent dose in colon was calculated as the mass-weighted average of the absorbed dose in the upper large intestine and lower large intestine (Tapiovaara & Siiskonen 2008) (Table 3).

Table 3. Irradiated fractions of tissues for the equivalent dose calculation.

Tissues (*Ti*)	f_i
Active bone marrow	
Mandible	0.028
Calvaria	0.056
Cervical vertebrae	0.027
Thoracic vertebrae	0.17
Clavicles	0.008
Ribs and sternum	0.192
Lumbar vertebrae	0.098
Sacrum	0.333
Brain	1
Salivary glands: Parotid, Submandibular gland, Sublingual gland	1
Thyroid	1
Esophagus	1
Breasts	1
Lung	1
Stomach	1
Liver	1
Colon: Upper large intestine (0.57)[1], Lower large intestine (0.43)[1]	1
Skin (cerebral vessels):	0.05
Lens of the eyes, Cheek, Neck, Head (lateral and posterior)	
Skin (cervicocerebral vessels):	0.15
Lens of the eyes, Head (lateral and posterior), Cheek, Neck, Thyroid, Breasts, Midline shoulder.	
Remainder tissues	
Adrenals, Gall bladder, Heart, Kidneys, Pancreas, Small intestine, Gonads	1
Extra thoracic airway: Nasal sinuses, Trachea, and Pharynx	1
Muscle: Left and right orbit, Parotid, Center cervical spine, Sublingual gland and Esophagus	0.05
Lymphatic nodes: Extra thoracic airways (0.13)[1], Salivary glands (0.08)[1] Thyroid (0.05)[1], Esophagus(0.04)[1], Stomach (0.03)[1], Pancreas (0.15)[1], Gallbladder (0.10)[1], Lungs (0.07)[1], Total body (0.05)[1], heart (0.04)[1], Small intestine (0.25)[1], Gonads (0.01)[1]	1

[1]Weighting factor of tissue for calculating the equivalent dose from mean dose of organs

4.2.4 Statistical methods

Study I

The mean error of the energy dependence measurements was calculated from mean doses of three repeated measurements relative to the reference dosimeter dose on each photon energy point as

$$error\% = 1 - \left(\frac{D(RPLD)_i}{D_{(ref)_i}}\right)_{mean} x100 \quad (35)$$

where $D(RPLD)_i$ and $D(ref)_i$ are RPLD and the reference dosimeter doses at *i*th energy point.

The coefficient of variation % (*CV%*) was calculated for repeated dose measurements and is defined as

$$CV\% = \left(\frac{SD}{\bar{x}}\right) x100 \quad (36)$$

where $\bar{x}$ is the mean of the measured doses, *SD* is the standard deviation of the doses and is calculated as

$$SD = \sqrt{\frac{\sum(X_i - \overline{X})^2}{n-1}} \quad (37)$$

where *i* is *1,2,3…*, x_i is the measured dose and *n* is the number of the measured dose.

The dose linearity was examined using Pearson's correlation coefficient (r).

Study II

In study II, the correlation coefficients were calculated using Spearmann correlation analysis between both the maximum and mean *D* determined in vagina and DAP or ESE values, also between the maximum *D* and the patient diameter or the distance from the mother's back surface to fetus surface.

Study II and III

In study II and III, the combined standard uncertainty (u_C) for individual RPL was calculated according to Zoetelief *et al.* 2000, and IAEA 2007 using type A and

type B uncertainties. The type A standard uncertainty is obtained by the usual statistical analysis of repeated measurements and is reduced by increasing the number, *N*, of individual readings. The source of measurement uncertainty that cannot be estimated by repeated measurements is evaluated using type B uncertainties. The combined uncertainty (u_C) is calculated using combining variances, which are squares of standard deviations and is defined as

$$u_C = \sqrt{{u_A}^2 + {u_B}^2} \tag{38}$$

(IAEA 2007). In the present thesis, type A was calculated from the mean CV% of three repeated dose measurements of each dose level in the air, being 6% on average in the dose ranges used in the current study. Type B was expressed as the dose response variation in the used energy spectrum (1% for intravaginal measurements, 6% for CTA and DSA), estimate of angular dependence (6% for intravaginal measurements, and 1.3% for DSA), X-ray source variation (2.5% for intravaginal measurements, 0.5% for CTA and 1% for DSA). The standard uncertainty of the estimated dose $\sigma(D)$ in air for each measurement point was calculated as

$$\sigma(D) = \sqrt{\frac{u_C}{N}} \tag{39}$$

where *N* is the number of exposures. The effective dose uncertainty $\sigma(E)$ was calculated as

$$\sigma(E) = \sqrt{\sum \sigma(D_{f,T})^2} \tag{40}$$

where $\sigma(D_{f,T})$ is the uncertainty of each tissue contributing to the effective dose uncertainty. The partial derivative model (IAEA 2007) was used and $\sigma(D_{f,T})$ is calculated as

$$\sigma(D_{f,T}) = \frac{w_T}{n}\sqrt{{f_T}^2 \sum \sigma(D_{Ti})^2 + \sum {D_{Ti}}^2\, \sigma(f_T)^2} \tag{41}$$

where w_T is tissue weighting factor for effective dose calculation (see Table 1), *n* is the number of dosimeters with the same weighting, $\sigma(f_T)$ is uncertainty of the irradiated fraction of the tissue and D_{Ti} is the mean dose of each tissue in the *i*th simulation runs of the examinations (IAEA 2007).

5 Results

The various properties of the RPLD, such as energy and angular dependence, dose linearity, reproducibility, and fading effect, were determined for measuring medical radiation doses. In addition, the RPL dosimeter was applied in absorbed and effective dose measurements.

5.1 Properties of RPLD for measuring radiation doses in radiology

5.1.1 Energy dependence

The RPLD with tin filter was found to be accurate for measuring doses in the 50–125 keV energy range when dosimeters were irradiated in air. The dose response of the RPLD was linear down to 50 kVp with a 2.9% mean error compared with reference measurement doses and it began to decrease significantly at 40 kVp tube voltage and below. The dose response began to decrease already at 50 kVp tube voltage when irradiation was done on the surface of a PMMA phantom. The mean error was 3.6% compared with reference measurement at 50–125 keV energy (Figure 19).

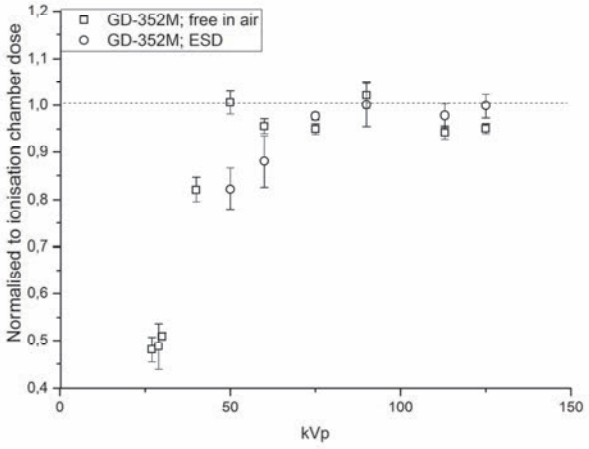

Fig. 19. Relative response of the RPL dosimeter normalized by the ionization chamber dose (dashed line) for typical X-ray photon energies used in radiology (published by permission of Oxford Journals).

5.1.2 Angular dependence

The angular dependence was not significant at angles between 0° and 40° in the vertical direction of the dosimeter, whereas it was 38.1% to +49.6% at angles above 50° (Figure 20).

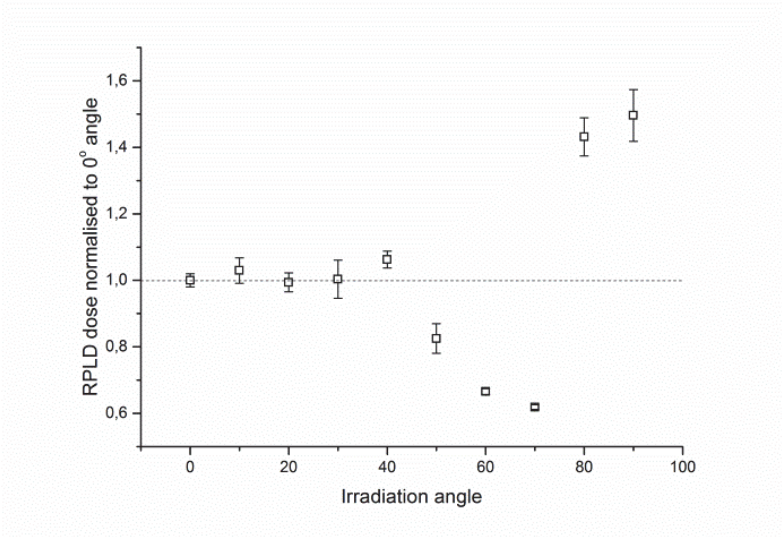

Fig. 20. The angular dependence of RPL dosimeter normalized to the reading of the horizontal axis at a 0º angle (dashed line), (published by permission of Oxford Journals).

5.1.3 Dose linearity

The RPLD shows excellent dose linearity ($R^2 > 0.99$) (Figure 21).

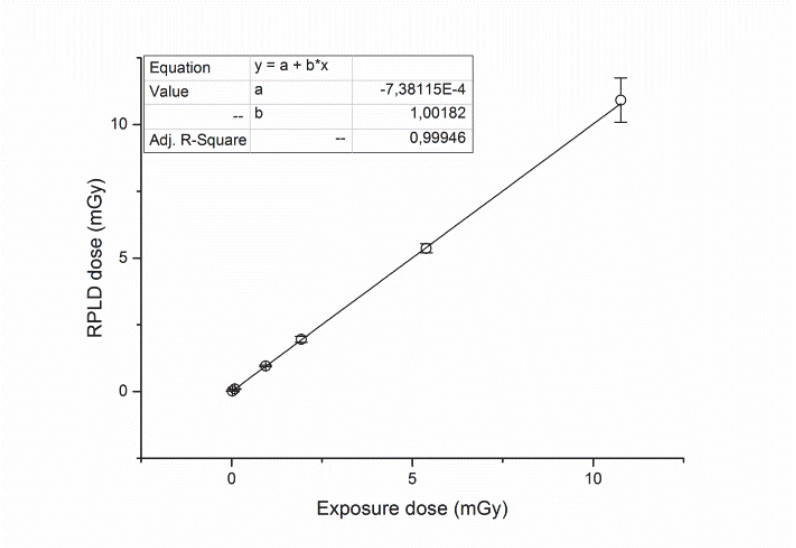

Fig. 21. The dose linearity of RPL dosimeter in the 20 µGy–11 mGy dose range (published by permission of Oxford Journals).

5.1.4 Reproducibility and fading effect

The lowest measured dose was 20 µGy and the CV was 12.2%. For low-dose measurements (20 µGy–11 mGy), it was 6% on average (Figure 22).

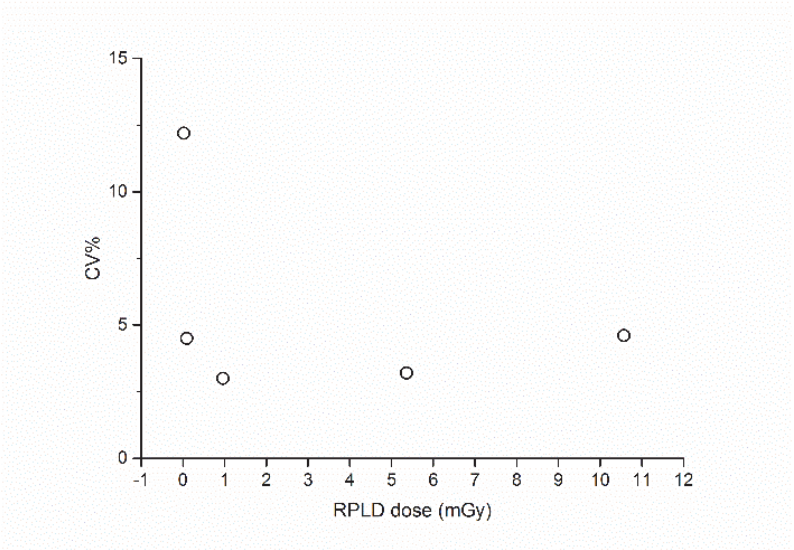

Fig. 22. The reproducibility of RPL dosimeters in the 20 μGy–11 mGy dose range.

Fading effect was negligible with a CV of 0.7% at room temperature in a 25-day follow-up in the 7 mGy–15 mGy dose range.

5.2 Absorbed doses from intravaginal measurements of the pregnant women during the prophylactic catheterization

To correct the dosimeter dose calibrated in air into the soft tissue dose, the vaginally absorbed doses (D) were multiplied by the ratio of the mass energy absorption coefficient, which was 1.06 for the tube voltage used in this study (Equation 16). For each patient, D was highest at the vaginal fornix and lowest next to the vaginal orifice (Table 4). The mean D calculated from the maximum doses for seven patients was 11.2 mGy (Table 5).

Table 4. The vaginally absorbed X-ray radiation doses (mGy) for the seven patients (published by permission of Springer).

Patient	No. 1	No. 2	No. 3	No. 4	No. 5	No. 6	No. 7
Dosimeter no. 1	4.9	10.5	4.1	15.8	28.7	12.4	2.2
Dosimeter no. 2	3.0	9.2	3.9	12.2	22.9	9.1	1.9
Dosimeter no. 3	2.1	6.1	3.3	6.4	14.9	4.5	1.1
Dosimeter no. 4	1.4	3.6	2.5	3.7	10.0	3.6	0.9
Mean	2.9	7.4	3.5	9.5	19.1	7.4	1.5
SD	1.5	3.1	0.7	5.5	8.3	4.1	0.7

Table 5. Radiation dose indicators for each patient due to the fluoroscopically guided endovascular treatment. (published by permission of Springer).

Patient	No. 1	No. 2	No. 3	No. 4	No. 5	No. 6	No. 7	Mean	SD
DAP($cGycm^2$)	626	1357	791	648	2001	1599	835	1122	535
ESE (mGy)	63	135	66	84	184	168	139	120	49
T_f (min:sec)	7:43	7:46	5:05	6:00	11:35	7:27	7:03	7:31	2:02
D_{max} (mGy)	4.9	10.5	4.1	15.8	28.7	12.4	2.2	11.2	9.1

The Spearman correlation coefficients between the mean D and DAP or ESE were 0.49 (P=0.27) and 0.47 (P=0.29), respectively. The Spearman correlation coefficients between the maximum D and DAP or ESE were 0.43 (P=0.34) and 0.46 (P=0.29) (Figure 23 and 24). The maximum D in vaginal fornix had no correlation with the patient's diameter. The Spearman correlation coefficient between the maximum D and patient diameter was 0.056 (P=0.90) (Figure 25). The Spearman correlation coefficient between the maximum D and the distance from the mother's back to the fetus surface was -0.32 (P=0.49) (Figure 26).

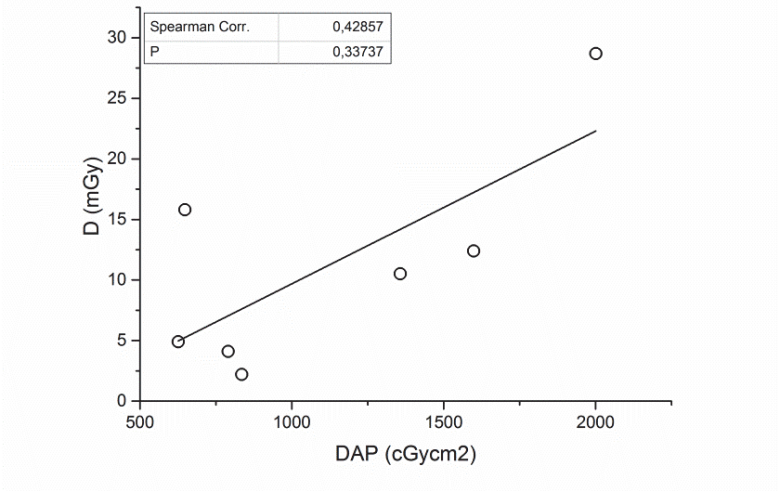

Fig. 23. The Spearman correlation between the maximum D and DAP (published by permission of Springer).

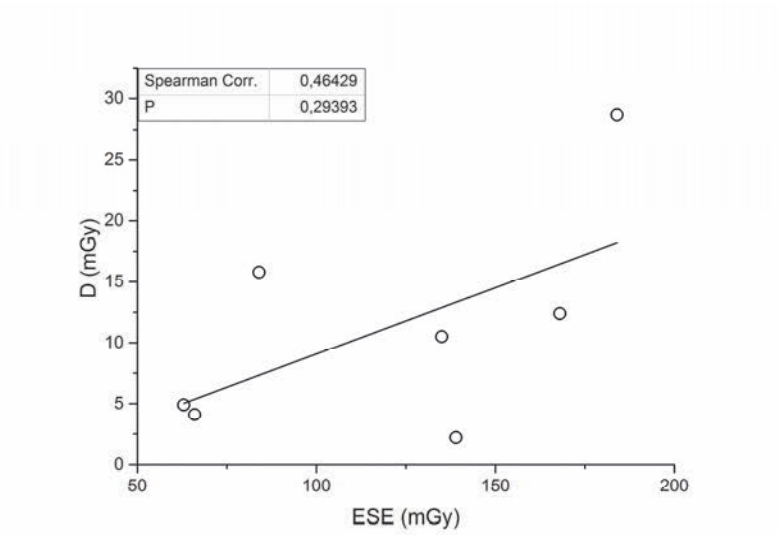

Fig. 24. The Spearman correlation between the maximum D and ESE (published by permission of Springer).

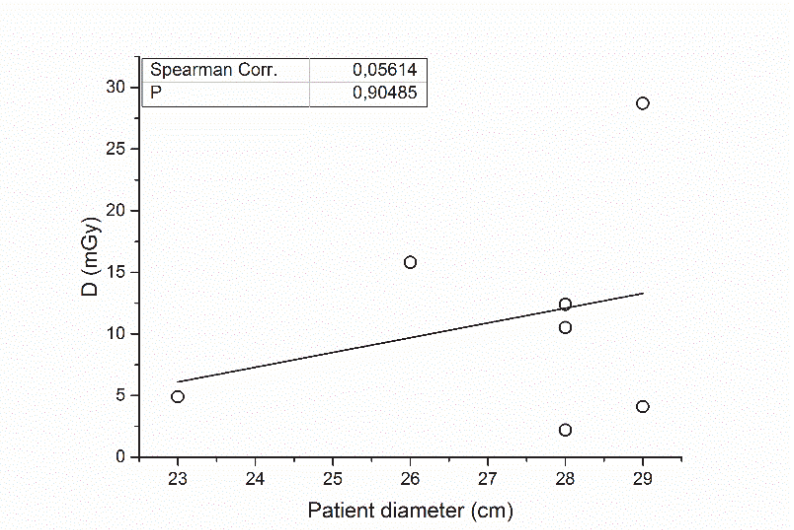

Fig. 25. The Spearman correlation between the maximum D and patient diameter.

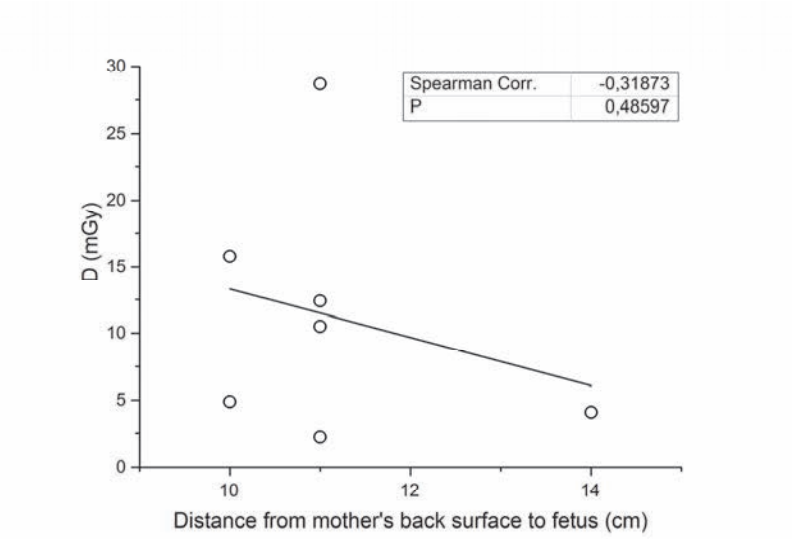

Fig. 26. The Spearman correlation between the maximum D and the distance from the mother's back to the fetus surface.

5.3 Comparison of the effective doses of CTA and DSA for a typical angiography of the cerebral and the cervicocerebral vessels

The present study showed, for cerebral vessels, that the effective dose for CTA was one-fifth the dose compared with DSA. In the imaging of the cervicocerebral vessels, the effective dose for CTA was approximately one-third higher compared with DSA. For the assessment of cerebral vessels, the absorbed doses in the head area for DSA were 2–7 times higher than those for CTA. The absorbed doses for the thyroid, thymus, and esophagus were somewhat similar, with low doses in these regions. For the assessment of cervicocerebral vessels, the absorbed doses in the head area for DSA were 2–3 times higher than those for CTA, whereas for the thyroid, thymus, and esophagus, the doses were higher in the CTA examination. The absorbed doses for the thoracic and abdominal region were higher in CTA than in DSA examinations. The mean equivalent doses to the active bone marrow are shown in Table 6 and to other organs and tissues in Table 7. The effective doses are given in Table 8 and conversion coefficients from DLP and DAP to the effective dose are shown in Table 9.

Table 6. The mean equivalent doses H_T (mSv) of active bone marrow for diagnostic angiography examinations of cerebral and cervicocerebral vessels.

Protocols and imaging area	CTA (AEC) Cerebral (mSv)	CTA (no AEC) Cervicocerebral (mSv)	DSA (AEC) Cerebral (mSv)	DSA (AEC) Cervicocerebral (mSv)
Active bone marrow (total):	1.12	5.38	5.48	6.24
Mandible	1.41	17.61	4.87	9.70
Calvaria	9.24	16.23	67.61	49.26
Cervical vertebrae	6.69	21.32	41.86	72.56
All thoracic vertebrae	0.43	7.37	2.04	6.43
Clavicles	0.45	15.27	1.48	3.35
Ribs and sternum	1.59	10.47	0.33	0.66
Lumbar vertebrae	-	0.06	-	0.03
Sacrum	-	0.02	-	-

Table 7. The mean equivalent doses H_T (mSv) of organs for diagnostic angiography examinations of cerebral and cervicocerebral vessels.

Protocols and imaging area	CTA (AEC) Cerebral (mSv)	CTA (no AEC) Cervicocerebral (mSv)	DSA (AEC) Cerebral (mSv)	DSA (AEC) Cervicocerebral (mSv)
Breasts	0.33	1.73	0.18	0.27
Colon	0.01	0.13	0.01	0.03
Lungs	1.03	7.91	0.68	1.41
Stomach	0.08	0.52	0.06	0.10
Ovaries	-	-	-	-
Liver	0.15	0.87	0.11	0.18
Esophagus	0.66	18.94	1.62	4.40
Thyroid	0.67	22.34	3.46	10.96
Urinary bladder	-	-	-	-
Brain	9.41	16.90	73.51	51.81
Adrenals	0.05	0.30	0.07	0.12
Extra thoracic airway	2.83	20.94	13.34	28.97
Gall bladder	0.07	0.47	0.06	0.11
Heart	0.54	3.27	0.32	0.57
Kidney	0.04	0.25	0.06	0.11
Lymphatic nodes	1.05	7.07	4.58	8.20
Muscle	0.28	0.91	2.92	3.57
Oral mucosa	5.95	20.53	31.13	42.61
Pancreas	0.02	0.19	0.02	0.03
Small intestine	-	0.07	-	-
Spleen	0.07	0.42	0.06	0.09
Thymus	0.53	14.67	1.66	5.10
Uterus	-	0.02	-	-
Skin:	0.42	2.24	2.61	4.62
Cheek surface, dexter	9.44	18.15	9.48	15.35
Neck surface, posterior	2.17	25.17	42.53	75.40
Skull surface, sinister	10.10	18.64	84.15	76.6
Skull surface, posterior	10.19	19.00	166.22	97.97
Midline shoulders posterior	-	13.66	-	30.75
Eyes (lens): dexter/sinister	9.13/9.00	13.70/14.45	6.52/6.86	4.68/5.39
Eyes (orbit): dexter/sinister	9.91/9.50	14.61/14.82	16.13/21.84	11.70/18.09

Table 8. The mean effective doses E (mSv) for diagnostic cerebral and cervicocerebral angiography examinations, the CV% is given in parentheses.

Protocols Imaging area	CTA (AEC) Cerebral[1] (mSv)	CTA (no AEC) Cervicocerebral[2] (mSv)	DSA (AEC) Cerebral[3] (mSv)	DSA (AEC) Cervicocerebral[4] (mSv)
ICRP 1990	0.66 (2.3%)	4.24	3.16 (1.3%)	3.40 (3.0%)
ICRP 2007	0.67 (1.9%)	4.85	2.71 (0.6%)	3.60 (3.6%)

Dose data from angiography imaging protocols: [1]$CTDI_{vol}$=14.1 mGy, DLP=262 mGycm; [2]$CTDI_{vol}$=12.3 mGy, DLP mGycm; [3]DAP=48.7 $Gycm^2$, [4]DAP=50.7 $Gycm^2$

Table 9. Calculated conversion coefficient from DAP and DLP to effective dose for diagnostic cerebral and cervicocerebral angiography examinations.

Conversion coefficients	CTA (AEC) Cerebral (mSv/mGycm)	CTA (no AEC) Cervicocerebral (mSv/mGycm)	DSA (AEC) Cerebral (mSv/$Gycm^2$)	DSA (AEC) Cervicocerebral (mSv/$Gycm^2$)
ICRP 1990	0.0025	0.0086	0.065	0.067
ICRP 2007	0.0026	0.0098	0.056	0.071

5.4 Uncertainties of dose measurements

The RPLD measurements in the anthropomorphic phantom indicated sufficient reliability in radiology. The coefficient of variation (CV) for three repeated simulation runs of the absorbed doses was on average 4.5% for CTA and 9.0% for DSA. However, CV% was only 0.6%–3.6% for the effective dose measurements for all examinations (Table 8).

In Study II, the combined uncertainty of an individual RPLD was determined to be 8.9% for the absorbed dose measurement in vaginal fornix and in Study III 8.5% for CTA examinations (Equation 38). For DSA examinations, it was 8.6%. If there were three repeated irradiation runs for one CTA simulation, the combined uncertainty at each measurement point was 4.9% (Equation 39).

The effective dose uncertainty was 7% for CTA and 11% for DSA examinations on average (Equation 40 and 41).

6 Discussion

The purpose of the current study was to assess the applicability of RPL dosimetry for dose determination in radiology.

First, the various properties of the RPLD were investigated to verify the applicability of the dosimeters for dose measurement in radiology.

Secondly, the absorbed dose measurement was carried out through the vaginal measurements for pregnant women undergoing fluoroscopy imaging during prophylactic catheterization before uterine artery embolization.

Thirdly, the measurement of the dose absorbed by the organs and the calculation of the effective dose were carried out using in-phantom measurements to evaluate the radiation exposure of two different angiography imaging methods, DSA and CTA of the cerebral and cervicocerebral vessels.

Finally, this study showed that RPLD can be used with sufficient reliability for radiation dose measurement in radiology. The various properties of the RPLD were observed to be suitable for *in vivo* absorbed dose measurements used in difficult circumstances estimating the absorbed dose in vaginal fornix. The implementation of in-phantom dose measurement using RPLD was shown to be accurate when comparing two angiographic imaging methods.

6.1 Radiation dose assessment using RPL dosimetry for measuring absorbed doses in radiology

The broad polychromatic spectrum of the X-ray sets the requirements for the characteristics of dosimeters used in radiology. Typically, the interaction phenomenon transferring energy to the tissue is photoelectric absorption at low energies less than 30 keV and Compton scattering at energies higher than 30 keV. The dosimetric properties are related to these interaction phenomena. The characteristics of the detector material must be close to the scattering and absorbing properties of the tissue.

6.1.1 Energy dependence

A characteristic of RPLD material is the over-response of the dose at low-energy photons less than 100 keV due to photoelectric absorption, see Figure 6 B (Perry 1987, Nishizawa et al. 2003, Hsu et al. 2007, Mizuno et al. 2008). This is due to the higher density (2.61 gcm^{-3}) and higher Z (12.0) compared to biological

tissues. In this thesis, we used an RPL dosimeter with a tin filter, which corrects the over-response at the energy range below 100 keV. The filter is located at both ends of the dosimeter's plastic capsule (Figure 12). In the current study, a flat response was observed to the typical X-ray energies for the RPLD using a tin filter, and a correction factor for energy dependence was not used.

Study I showed that RPLD with a tin filter has a linear response with a mean error of 2.9% in the 50 kVp–125 kVp energy range and 3.6% in the 60 kVp–125 kVp energy range measured in air and on the surface of the PMMA phantom. The results are consistent with earlier research (Nishizawa *et al.* 2003). Based on Study I, the error of the dose response was 18% at 40 kVp determined in air and 14.9% at 50 kVp on the surface of the PMMA phantom compared with ionization chamber dose. The dose reduction is partly due to the K-edge of tin at 29.1 keV (Dendy & Heaton 1999) and partly due to the thin plastic holder (Kadoya *et al.* 2012). This may cause error in organ dose measurements, especially for organs near the surface of the phantom, where the low-energy photons are absorbed. The error is presumably decreased with organs located deeper in the body, because the beam hardening effect increases the mean energy of the X-ray spectrum by filtering out the low-energy photons when thicker objects and especially bone structures are exposed. In Study II, the bone structure in the pelvis of the mother absorbed low-energy photons in vaginal measurements and caused a higher effective energy spectrum, which is to be detected in sufficient reliability by RPLD according to this thesis.

The response of RPLD with an energy compensation filter was flat from 45 keV to 60 keV, however, without the filter the response varied about 20% and was three to four times higher than the response with tin filter in the diagnostic energy range (Perry 1987, Nishizawa *et al.* 2003, Hsu *et al.* 2007, Mizuno *et al.* 2008). Because of the variable dose response depending on effective energy and remarkably high over-response in energies less than 100 keV, the RPLD without tin filter must be calibrated to every effective energy. This may cause problems due to the variable tube voltage, i.e. fluoroscopy and DSA, when the tube voltage is automatically adjusted depending on patient size, or in the case of two X-ray tubes used in biplane angiography equipment (Nishizawa *et al.* 2008). These are the reasons why RPLD with tin filter was used in the current thesis.

In Study I, the sensitivity of RPLD for detecting the entrance surface dose decreased less than 50 kVp compared with the ionization chamber dose. This may cause underestimation in detecting scattered radiation. In the current thesis, BSF could not be estimated accurately for DSA and CTA with different irradiation

geometries and parameters. Furthermore, BSF varies greatly when using varying fields of view and also different X-ray energy spectra (Benmakhlouf *et al.* 2011). BSF is used in circumstances when incident air kerma is converted to entrance surface air kerma. Another situation is where organ doses are calculated using conversion coefficients based on incident air kerma (IAEA 2007). In Study I, ESD measurements for RPLD showed sufficient reliability down to 50 kVp, which is consistent with earlier investigations (Nishizawa *et al.* 2003)

6.1.2 Angular dependence

The construction and physical size of RPLD dosimeters, the energy of the incident radiation, and a variable beam direction relative to dosimeter during the exposure are the main sources of angular dependence, i.e. fluoroscopy-guided treatment or during DSA examinations. In actual measurements, dosimeters should ideally be used in the same geometry as they were calibrated (Perry 1987). Angular dependence has not previously been studied in the vertical direction for a cylinder-shaped RPLD with a tin filter. In Study I, a variation of the dose was noticed particularly at great angles. The tin filter ring with a hole in the vertical direction of the dosimeter (Figure 12) is located at both ends of the dosimeter. In the present study, we found that tin absorbs photons more efficiently at 50°–70° angles than in the horizontal direction of the dosimeter, and dose reduction is detected. From the vertical direction of the dosimeter, the hole lets radiation in and the dose response is highly increased.

Additional measurements were performed to verify the accuracy of the vaginal dose (data not shown). The dose reduction due to the angular dependence was observed to be about 35% at 50° and 60° angles at 40 kVp inside the PMMA phantom in the depth of 14 cm. This error was found to be compensated by scattered radiation when shifting to higher energies. The mean error was found to be about 6% at 50°–70° angles, and in the worst case it was 10% at a 70° angle at 60 kVp. The scatter due to Compton effect increases with increasing energy. The scattered photon direction is nearly the same for each scattered angle at low energies 20 to 30 keV, and a forward angle is somewhat favored in the diagnostic ranges as energy increases (Dowsett *et al.* 2006). The scattered radiation is assumed to be the main source of the compensation of the dose underestimation due to the angular dependence inside the phantom (unpublished data).

In the current thesis, the angular dependence was taken into account, placing the long axis of the dosimeter perpendicularly to the photon beam. In Study III,

during the phantom measurement, RPLDs were placed along the z-direction in holes inside the phantom and on the phantom surface. Also, in the custom-made paraffin breast insert, the holes for dosimeters were made in the z-direction. In Study II, during the intravaginal measurements, RPLDs were placed in plastic tubes in vaginal fornix (Figure 15). The long axis of the dosimeter was then placed perpendicularly to the photon beam within the limits of the patient's anatomy and position on the table. Based on the results of Study I, the angular and energy dependence of the RPLD at low energies caused some underestimation of the doses. In Study II, fixed 92 kVp tube voltage and 3 mm Al filtration with additional 0.3 mm Cu filtration were used. The effective energy of the beam quality used in Study II was 50–60 keV, and the number of photons at less than 40 keV is low (Figure 13). This minimizes the angular and energy dependence error in Study II. The mean estimated error is approximately 6% at 50°–70° angles at 60 kVp (data not shown).

The angular dependence is a potential source of error in the oblique projections of cranio-caudal direction, which were used in fluoroscopy and in DSA examinations in Study III. However, frames from the oblique projections were about 23% of the total examination frames and its influence is negligible in the 70–90 kVp energy range in Study III. In CTA, the error is negligible because of the high 100–120 kVp energy range and high tube filtration in CTA. In both imaging techniques, the error is possible when dosimeters are at the boundary of the primary beam.

6.1.3 Dose linearity and reproducibility of the measurements

In Study I, excellent dose linearity (R^2=0.99) was found for doses between 20 μGy and 10 Gy. The result is in line with previous studies (Perry 1987, Nishizawa *et al.* 2003, Hsu *et al.* 2006, Hsu *et al.* 2007, Ihara *et al.* 2008, Lee *et al.* 2009, Rah *et al.* 2009a). Based on the results in Study I, the low dose detection limit was found to be 20 μGy with a CV of 12.2%. The characteristic of detecting very low doses is particularly important in radiology when radiation exposure from the primary beam is detected. In Study I, good accuracy and reproducibility were observed at very low dose measurements (20 μGy–11 mGy) with an average coefficient of variation of 6%. Previously, a CV of 0.5–2% (600 μGy–5 Gy) has been reported (Hsu *et al.* 2006, Hsu *et al.* 2007, Lee *et al.* 2009, Rah *et al.* 2009a).

6.1.4 Fading effect

RPLD was found to have minimal fading effect. This is an advantage over the commonly used TLD, which has a characteristic of dose fading when stored at room temperature. The negligible fading of the dose absorbed to the RPLD material is due to the stable luminescent centers of Ag^0 and Ag^{++} ions. When the dosimeters are heated after irradiation, the luminescent centers remain relatively constant (Perry 1987, Hsu *et al.* 2006, Knezevic *et al*. 2013). In Study I, dosimeters were preheated at 70°C for 30 minutes and stored in room temperature 25 days after irradiation to observe the fading effect. Based on the results of Study I, the fading effect was negligible with a CV of 0.7% at low dose ranges, which is consistent with other investigations (Perry 1987, Hsu *et al.* 2006, Knezevic *et al.* 2013). The fading effect was found to remain stable up to 50°C (Perry 1987), which is important in the assessment of *in vivo* measurements. RPLD also permits repeated measurements free from the fading effect, allowing repeated read-out, resulting in more accuracy (Perry 1987, Piesch *et al.* 1993, Hsu *et al.* 2006). This characteristic of RPLD is superior to TLD, because TLD's dose fades in the read-out procedure (Oberhofer & Scharmann 1993).

In summary, the properties of RPLD with tin filter are sufficient for low-dose measurements and the continuous spectrum of the X-ray when energies between 40 kVp and 125 kVp are used.

6.2 Clinical applications of RPL dosimetry

In the case of mortal danger or risk of bleeding, infection, and pregnancy loss, embolization was observed to be a safe treatment, although some radiation exposure must be accepted to the fetus due to the fluoroscopy-guided endovascular procedure (Ojala *et al.* 2005, Uchiyama *et al.* 2008, Wortman *et al.* 2013). The dose evaluation is recommended, when the dose to the fetus is estimated to be greater than 10 mGy (Dauer *et al.* 2012). A suitable dosimetry method is needed for reliable measurement *in vivo*.

The application of specific dose quantities is useful for the optimization of image protocols and comparing image modalities. Determining absorbed and effective doses is a suitable approach for estimating tissue reactions and stochastic effects (IAEA 2007). In Study III, the estimation of tissue reactions was determined by using a direct dose measurement approach. The entrance surface dose was determined by laying RPL dosimeters on the surface of the phantom to

measure the local dose to the eyes and skin. The effective dose is an appropriate method for comparing the stochastic effect of different procedures. In the present study, when assessing the stochastic effect of the radiation exposure in cerebral and cervicocerebral DSA and CTA examinations, the mean values of the equivalent dose of the radiation-sensitive organs and tissues were determined. Because direct dose measurements of several organs cannot be performed on patients, an anthropomorphic phantom was used.

6.2.1 In vivo absorbed dose measurement

The aim of medical exposures is to keep the radiation exposure for the patient as low as reasonably achievable (ALARA). Because fluoroscopy- and CT-guided interventional procedures in the pelvic area, for example, may deliver doses higher than the developmental disorders threshold, which is estimated to be 100 mGy, individual justification of radiological examinations and treatments is needed (McCollough *et al.* 2007, Dauer *et al.* 2012). Also, when the dose to the fetus is estimated to be greater than 10 mGy, more accurate dose assessments are recommended (Dauer *et al.* 2012). The purpose of Study II was to determine the radiation dose in vaginal fornix during fluoroscopically-guided prophylactic catheterization of the anterior trunks of internal iliac arteries before uterine arterial embolization. The treatment prevents massive anticipated bleeding and death of mother and fetus. The absorbed dose results can be used for evaluating the radiation exposure in the area near the fetus, where the radiation was used most of the time during the catheterization. The special interest was in the absorbed dose to the fetus, not to the mother. In fluoroscopy, radiation exposure is affected by various factors, such as the diameter of the mother, the direction of the projection, the depth of the fetus from the skin surface, X-ray technique factors, and operator experience (Andrews & Brown 2000, Nicolic *et al.* 2001, Mooney *et al.* 2001, McCollough *et al.* 2007, Brisse *et al.* 2009, Dauer *et al.* 2012). The dose to the fetus may vary by a factor of 10 for a specific examination (McCollough *et al.* 2007). In Study II, the variation of the same amount was observed between the absorbed doses with different patients.

The doses to the fetus in abdominal radiographic examinations have previously been estimated by using phantom models with Monte Carlo methods. These methods use beam characteristics, such as kVp, total filtration values, and field size, to estimate organ or fetus doses within approximately 10%–50% accuracy (Dauer *et al.* 2012). Estimating organ doses can also be based on

entrance skin dose or kerma air product (DAP) measurements. These methods are appropriate during the first trimester, because the fetus dose may be assumed to be approximately equal to the uterus dose (Dauer *et al.* 2012). The underestimation of the scattering phenomena within the patient causes some inaccuracy with these methods. In addition, the models that do not use patient-specific fetus depths may overestimate or underestimate doses by up to 80% (Dauer *et al.* 2012). Furthermore, the X-ray tube position relative to the patient may change numerous times during the examination, and radiation is applied intermittently at different times during the study; the Monte Carlo-based method may thus be difficult to use. Furthermore, automatic exposure control (ABC) adjusts the beam output continuously based on the patient diameter and type of tissues. The exact imaging parameters are difficult to detect during the examination. The use of Monte Carlo method is thus not appropriate (Dauer *et al.* 2012).

Previously, direct dose measurements were used for absorbed dose measurement for uterine artery embolization for leiomyomas (Nicolic *et al.* 2001, Glomset *et al.* 2006). The somewhat different absorbed dose values compared with the current study were due to the use of a different imaging technique employing angiographic exposures (Nicolic *et al.* 2000, Glomset *et al.* 2006, Nishizawa *et al.* 2008). In these studies, an absorbed dose of 22 mGy–652 mGy was estimated for ovary dose, which is up to 20 times higher than measured in the present work.

The significant difference was revealed with dose levels between the two dose detection methods for estimating the uterine doses during the UAE procedure (Glomset *et al.* 2006). Further, the author estimated the uterus dose using a method based on measuring air dose corrected by backscattered radiation at the skin surface. The calculation of the organ dose as a function of organ depth was based on inverse square law corrections and normalized depth dose in phantom. Skin surface dose was measured from seven TLDs. The comparison method was based on vaginal measurements for the same 13 patients (Glomset *et al.* 2006). This investigation revealed that the vaginal measurement gave 36% smaller absorbed doses on average than the calculation method underestimating the uterus dose. During the UAE treatment, the angiographic exposures are focused on uterine arteries and on the uterus (Nishizawa *et al.* 2008), where leiomyomas are located in different patients. In addition, the method using organ dose calculation compared with skin surface dose measurements may overestimate the uterus dose due to the inverse square law corrections. This

method may not accurately reflect the influence of the bone structure of the pelvis, which greatly absorbs the radiation from the X-ray tube located under the table. The UAE procedure differs from the catheterization procedure used in Study II. In the previous studies, the absorbed dose from both the catheterization and the embolization treatment is included in the detected doses (Nicolic *et al.* 2000, Glomset *et al.* 2006, Nishizawa *et al.* 2008). The doses from the embolization of the uterine arteries were excluded in Study II, because the delivery of the infant was done before the embolization and doses were detected only during the catheterization. In addition, the catheterization technique for the pregnant women in Study II considerably differs from previously reported studies, which were carried out on non-pregnant older women diagnosed with leiomyomas. In study II, the catheterization of the pregnant women was done using low-dose fluoroscopy exploiting LIH images and using small collimation to prevent the exposure to the fetus. Also, relatively young patients in Study II were easier to catheterize. This is evident from the fluoroscopy times, which were two or four times higher in previous studies (Nicolic *et al.* 2000, Glomset *et al.* 2006, Nishizawa *et al.* 2008).

In Study II, the catheters were introduced rapidly into the proximal parts of the internal iliac arteries using intermittent fluoroscopy imaging. Then, an angiography catheter was advanced into the anterior trunks of both internal iliac arteries and catheters were fixed (see Figure 14). The correct position of the catheter was checked using a small bolus of contrast medium and low-dose pulsed fluoroscopy imaging. The most part of the radiation exposure was focused on the anterior trunks of the internal iliac arteries, not on the uterus. The uterine arteries are small arteries and the catheters were fixed into the anterior trunks of both internal iliac arteries to prevent the embolization of the uterine arteries before delivery. This is important for protecting the oxygen supply of the fetus.

Since dose metrics from the imaging equipment (e.g. DAP, ESE, T_f) only reflect the patient's radiation exposure in general, specific parameters, such as varying collimation and dose rate, were difficult to follow exactly. Consequently, the absorbed dose measured directly from the vaginal fornix was used to estimate the absorbed dose in the area near the fetus in Study II. Based on a literature search, the absorbed dose measured directly in the vagina has not been previously published for pregnant women.

In Study II, the absorbed dose showed a trend between other dose metrics, although statistical significance was not reached (Figure 23 and 24). This is probably due to the varying location of the FOV relative to the position of the

dosimeters, and to the varying absorption of photons by adjacent tissues between different patients, as well as to the small sample size. The diameter of the mothers varied from 23 cm to 29 cm and the distances from the mothers' back to the fetus surface varied from 10 cm to 14 cm. In Study II, the X-ray tube was placed under the table on the posterior side of the mother. This method protects the unborn child because the mother's body absorbs the lower energy photons. X-rays attenuate more effectively in bone than in an equal volume of soft tissue due to the higher Z_{eff} and physical density of bone. This is the reason for reduced doses behind bone (Hendee & Ritenour 2002). The fetal absorbed dose may be reduced by a factor of 16 by using a PA projection instead of the corresponding AP projection (Ragozzino *et al.* 1981).

In Study II, the correlation between D and DAP did not reach statistical significance. One explanation for the lack of correlation is that the beam was not directed to the vagina area throughout the catheterization. The maximum dose in all cases was measured from the dosimeter located in vaginal fornix next to the fetus head during the whole examination. The measurement can therefore be considered as an estimate of absorbed dose near the head of the fetus. The fetus was in an occiput position in all cases.

In Study II, to correct the dosimeter dose calibrated in air into the soft tissue dose, the vaginally absorbed doses were multiplied by the ratio of the mass energy absorption coefficient, which was 1.06 for the 92 kVp X-ray tube voltage used in this study (Hubbell & Seltzer 1996). An uncertainty of 7% in dosimeter reading is sufficient for assessing the potential risk of pediatric examinations (IAEA 2007). Based on the results of Study I, the combined uncertainty was calculated to be 3% for the individual RPLD used in intravaginal measurements. When considering the angular dependence error and the tube output variation, the combined uncertainty is calculated to be 8.9% (data not shown).

6.2.2 Absorbed dose measurements using phantom

In Study III, the absorbed doses to the skin, brain, salivary glands, and eyes during diagnostic CTA and DSA examinations did not reach the tissue reactions threshold. According to ICRP, an absorbed dose of up to about 100 mGy does not generate clinically relevant functional impairment for any tissue (ICRP 2007). The threshold value for opacities of the lens is 500–2000 mGy, and for skin epilation or temporary hair loss, 2000–3000 mGy (ICRP 2007).

Based on Study III, when imaging cerebral vessels, the organ doses over the primary beam area with CTA were lower compared with DSA. This is the consequence of the different imaging parameters and geometry between the two techniques. Furthermore, on CT scanners the filtration of the primary beam is typically stronger compared with angiographic devices, resulting in a harder irradiation spectrum. Therefore, radiation is more penetrating, and a smaller amount of low-energy photons is absorbed in tissues with CTA. During a CTA examination, radiation is distributed more evenly over the irradiated area than in a DSA examination, where irradiation is divided between two planes: anterior-posterior and lateral projections. This is seen in the entrance surface doses on the posterior side of the skull. With DSA examination, the dose on the skull surface was 20 times higher than with CTA examination. The same is observed in the brain dose, but the difference in doses is smaller. The absorbed doses for the orbits were nearly the same with both imaging techniques. This is probably a consequence of the strong attenuation of the radiation in the posterior direction in the skull and brain. The attenuation in lateral projection is smaller in DSA, but the number of frames in this direction is about 23% of the total frames used in DSA. The difference between doses between right and left orbits is due to the direction of the X-ray tube in DSA. For the DSA examination, the entrance surface dose for the lens was smaller than the dose for orbits and is probably a result of the irradiation geometry since the dosimeters were at the boundary of the primary beam in the lateral direction.

In the assessment of cervicocerebral vessels, the absorbed doses in the thyroid, thymus, esophagus, and lungs were higher with the CTA procedure than with DSA. The higher organ doses with CTA are probably due to a different irradiation geometry compared with DSA, so that there are more radiosensitive organs in the primary beam with CTA than with DSA. The entrance surface doses were similar for CTA and DSA due to imaging geometries and the direction of the X-ray tube in DSA.

6.2.3 Determination of effective dose using phantom

Study III compared the radiation exposure due to DSA versus CTA for the diagnostic assessment of cerebral and cervicocerebral vessels by using the same dose determination technique. Effective dose facilitates the comparison of stochastic effect between different types of diagnostic examinations or those having different acquisition parameters. In Study III, the same phantom and

dosimeters were used for each simulation run for different imaging modalities. While phantom measurements provide dose data in an average-sized patient, for such a comparative approach, the use of a phantom yields the most comparable data, since the error caused by different sized patients is minimized. Mean absorbed dose of the organs was determined for calculating the effective dose. Both old and new organ weighting factors of the ICRP were used for the effective dose determination of DSA and CTA (ICRP 1990, ICRP 2007).

The effective atomic number of the medium has a significant role in the interaction with photon radiation. In Study III, an anthropomorphic phantom (Alderson-Rando Phantom) was used. The composition of muscles and internal organs was considered similar to soft tissue in Study III. Muscle tissue has greater electron density than air, but the attenuation of X-ray photons for muscle exceeds that for air, and the difference is minimal with photons less than 100 keV (Hendee & Ritenour 2002).

Previously, the breast has been assumed to have the composition of fat (Jones 1997). In Study III, paraffin was used for breast inserts. However, the breast in the body is partly formed of fat and partly of soft tissue, which caused minor underestimation of the breast dose in the current study. This difference is seen in the mass energy absorption coefficient of the breast (Figure 3 A). Fat is a more penetrable medium for low-energy photons than an equal mass of soft tissue or bone due to the lower Z_{eff} (Hendee & Ritenour 2002). Furthermore, the electron density of hydrogen is about twice that of other elements, and more Compton interactions occur in fat than in an equal mass of muscle or bone (Hendee & Ritenour 2002).

It is assumed that the active bone marrow absorbs energy per gram as efficiently as bone. This is correct at 200 keV or more, but at energies below 100 keV it overestimates the dose to the active bone marrow due to the photoelectric effect of the photon interaction process (Cristy & Eckerman 1987). The active bone marrow consists of blood cells and fat, and interaction is comparable to soft tissue (Figure 3 A).

Because the effective dose is calculated through the mean absorbed doses of the organs, the dose measurements must be as accurate as possible. Depending on the organ volume, 1–9 dosimeters were placed in the organ in the same positions with both imaging methods to ensure the accuracy. Also, depending on the acquisition protocol, the phantom was equipped with at least 69 RPLDs. When simulating the imaging protocols, three repeated acquisition and mean values of the acquisition runs were used to decrease the inaccuracy. Furthermore, the

phantom position was adjusted with laser light to ensure the same position between the CTA simulation runs. In the DSA examination, it was not possible to use laser light when adjusting the phantom position, which is why the position of the phantom was adjusted by the radiologist using fluoroscopy. The CV% between simulation runs was 4.5% for CTA on average and 9.0% for DSA on average.

In Study I, the reproducibility of the RPLD in 20 μGy–1 mGy doses is inferior to that at higher than 1 mGy doses. Therefore, individual background doses caused by the predose of each dosimeter were measured before loading dosimeters into the phantom. These background doses were subtracted from the individual irradiated dosimeter doses to improve measurement accuracy particularly at the low dose limit level. The control dosimeters showed the natural background to be negligible, at less than 10 μGy, and it was ignored in the results. Based on Study I results, the deviation between dosimeters was negligible, less than 1.4%, and individual calibration of the dosimeters was not needed. Also, CV% was 0.3% on average after ten repeated read-outs of dosimeter dose. These results were consistent with those of a previous investigation (Hsu *et al.* 2006, Knezevic *et al.* 2013). Since RPLD manifested good repeatability and the position of the individual dosimeters in the phantom was the same in all simulations, the higher inaccuracy of the absorbed doses between repeated simulations of DSA examination was probably due to the positioning of the phantom. This inaccuracy in absorbed dose measurements did not cause significant error in the effective dose calculations. CV% was between 0.6% and 3.6% in Study III, see Table 8. To estimate relative radiation risks associated with various procedures for comparative dose measurements, the uncertainty of 7% is acceptable. In cases of low organ dose, the accuracy of 20% is acceptable (IAEA 2007). In the current thesis, the effective dose uncertainty was calculated to be 7% for CTA and for 11% for DSA examinations, which is sufficient to the comparative dose measurements. The setup in Study III provides comparable and objective information on the radiation exposure due to CTA and DSA. The effective dose for both CTA examinations of cerebral and cervicocerebral vessels were determined by a Monte Carlo-based CT-EXPO program to verify the phantom method. The effective dose from phantom simulations using anthropomorphic phantom and RPLD was consistent with CT-EXPO. The Monte Carlo method gave a 6% higher effective dose to both CTA examinations.

In the assessment of cerebral vessels, the effective doses for CTA are reported as 1.9 mSv (Cohnen *et al.* 2006) and 0.5 mSv (Struffert *et al.* 2014) using TLD

and anthropomorphic phantom. In Study III, the corresponding doses were 0.66 mSv (calculated with weighting factors of ICRP 1990) and 0.67 mSv (calculated with weighting factors of ICRP 2007). The longer scan length in the study by Cohnen *et al.*, reaching radiosensitive organs in the body area, was one reason for the difference compared to the present work. In a recently published study, a higher tube voltage was used than in the present study, but the effective tube current-time product was similar (Struffert *et al.* 2014). The lower effective dose determined by Struffert *et al.* compared with the present study is due to a 9 cm shorter scan length. In the assessment of cervicocerebral vessels, the effective dose was determined to be 3.3 mSv (Struffert *et al.* 2014), while it was 4.9 mSv in the present work. The tube voltage and tube current-time product was the same in both studies, but scan range was 10 cm longer in the present work, resulting in a higher effective dose. The scan length is a major source of the higher effective dose due to more radiation sensitive organs being exposed to the primary radiation.

In Study III, in the assessment of DSA examinations, the number of images acquired was that typically used to produce sufficient information for diagnosis. If more images are required with difficult cases, DAP and E will increase by the same factor when irradiation is directed to the same area of the body. In such a case, a conversion coefficient can be used for the E calculation of the same irradiation area. In Study III, a conversion coefficient of 0.056 mSv/Gycm^2 was determined for calculating E for the DSA examination of cerebral vessels. A recently published study used it for the estimation of E. The radiation exposure for diagnostic DSA of the patients ranged from 2.9 to 10.1 mSv (mean 6.3 mSv), being highly variable due to the variation in fluoroscopy time, number of vessels, and number of frames acquired for the examination of different patients (Fujiwara *et al.* 2013). In Study III, the diagnostic DSA for cerebral vessels resulted in a 2.7 mSv effective dose using the phantom method and is an estimate of the patient's stochastic effect for a particular imaging area and imaging procedure, which consists of a particular number of frames and projections.

In Study III, a low stochastic effect for CTA procedures of the cerebral vessels was found. The effective dose is five times lower than that in the same examination with DSA. Similarly, the organ doses over the primary beam area in CTA were lower compared with DSA. The higher stochastic effect for a DSA procedure of the cerebral vessels was strongly dependent on higher absorbed doses in the head and neck area. In Study III, the DAP to effective dose conversion coefficients for a cerebral DSA examination were 0.065 (ICRP 1990)

and 0.056 mSv/Gycm^2 (ICRP 2007), which are somewhat smaller compared with those in a previous report (Bridcut *et al.* 2007). The difference between conversion coefficients is probably due to the different determination method (Monte Carlo) used by Bridcut *et al.* In Study III, the conversion coefficients for a cervicocerebral DSA procedure were 0.067 (ICRP 1990) and 0.071 mSv/Gycm^2 (ICRP 2007) and are somewhat higher than those for the cerebral examination, due to the exposure to radiation-sensitive organs in the cervical and thoracic area (i.e., thyroid, thymus, sternum, esophagus, and lungs). To our knowledge, the conversion coefficients for cervicocerebral DSA examinations have not been published previously.

Since the ICRP published the new weighting factors, only a few conversion coefficients have been published (Wrixon 2008, Deak *et al.* 2010, McCollough *et al.* 2010, Christner *et al.* 2010). The ICRP has provided the conversion coefficients for different locations of the body for CT examinations determined by Monte Carlo calculation. The conversion coefficient for the brain is 0.0023 mSv/mGycm (ICRP 1990). In Study III, the calculated conversion factors 0.0025 mSv/mGycm, (ICRP 1990) and 0.0026 mSv/mGycm, (ICRP 2007) for the CTA of the cerebral vessels were used with the phantom method. The difference between conversion coefficients is probably due to different determination methods; differences between virtual (Monte Carlo) and actual phantoms, tube current modulation technique, and scan length.

The imaging technique and parameters used in CTA scanning for cervicocerebral vessels is one reason for the higher effective dose compared with the same examination acquired with DSA. The tube voltage, tube current, and scan speed must be kept high enough to acquire images with sufficient quality and to maintain image resolution comparable with that in DSA. Also, thin slice thickness is necessary to avoid partial volume artefacts. These imaging parameters improve spatial resolution and increase radiation exposure. While CTA provides high image quality, DSA is still generally considered the criterion standard. Differences between the image quality of DSA and CTA are explained by the vessel-to-background ratio and are enhanced in DSA due to the subtraction technique, eliminating undesirable image information. The DSA technique enables the use of lower tube voltage and tube-current time product than CTA. With DSA procedures, the number of images acquired contributes to the increasing radiation exposure of the patient.

After the development of the bone subtraction technique, the multi-slice CT technique has become the primary method for evaluating intracranial aneurysms

(Tomandl *et al.* 2006, Romijn *et al.* 2008, Sakamoto *et al.* 2006, Watanabe *et al.* 2008). Bone subtraction techniques require two volume acquisitions (Watanabe *et al.* 2009). This results is an approximately 27% higher dose than conventional CTA which is carried out with one acquisition (Lell *et al.* 2007). Recently, a CT system with a dual energy source has been developed. Dual energy CTA performing with only one acquisition using two tubes and energies has been reported to achieve similar diagnostic image quality at a lower radiation dose than digital subtraction CTA with high sensitivity and specificity compared with 3D DSA (Zhang *et al.* 2010). The radiation dose, however, remains an important issue to be resolved due to the different CTA acquisition techniques as compared with DSA.

Effective dose is commonly used to allow a comparison of the stochastic effect associated with different spatial dose distributions produced by different imaging techniques. In Study III, this method was used because of the difficulties involved in comparing different imaging techniques and the radiation exposures between different quantities. Furthermore, the risk assessments for different imaging techniques are often made using effective dose. Recently, the need for a quantity to simply compare the risks from a different distribution of inhomogeneous dose has been identified (Brenner 2008). Instead of multiplying organ doses by tissue-specific weighting factors, multiplying organ doses by the best-available, organ-specific lifetime cancer risks would be a better way. This effective risk would then be a lifetime radiation-attributable cancer risk. Furthermore, the effective risk is dependent on age at exposure time. This could be used as pediatric risk, adult risk, or all-ages risk (Martin 2007, Brenner 2008). This is a very interesting concept, but the determination of effective risk is not yet in common use.

7 Conclusions

This study investigated the applicability of radioluminescence dosimeters (RPLD) for determining absorbed and effective doses in radiology. RPL dosimetry was revealed to be a sufficiently reliable method to estimate both the absorbed radiation doses in *in vivo* measurements and for effective dose determination in phantom.

The main conclusions from the present thesis are summarized as follows:

1. The RPLD shows excellent dose linearity, minimal fading, good reproducibility, and excellent batch uniformity. The methodology is independent of photon energy in the energy range used in radiology.
2. The radiation exposure determined in vaginal fornix during the prophylactic catheterization of the pregnant women was shown to be a low-dose study when pulsed fluoroscopy with an optimized protocol was used without angiography exposures.
3. The radiation exposure was determined for a typical four-vessel angiography of the cerebral area, including intracranial vessels, and for the cervicocerebral area, including both cervical and intracranial vessels. CTA examinations for the cerebral vessels yield a five times lower effective dose for the patient than the corresponding examination performed with DSA. Cervicocerebral CTA, however, causes a one-third higher effective dose compared to the corresponding examination with DSA. Conversion factors derived from the data can be used to estimate the effective dose in both CTA and DSA of cerebral and cervicocerebral vessels.

References

AAPM (2008) American Association of Physicist in Medicine. The Measurement, Reporting, and Management of Radiation Dose in CT. AAPM 96.

Andrews RT & Brown PH (2000) Uterine Arterial Embolization: Factors Influencing Patient Radiation Exposure. Radiology (217): 713–722.

Araki F, Ikegami T, Ishidoya T & Kubo HD (2003) Measurements of Gamma-Knife helmet output factors using a radiophotoluminescent glass rod dosimeter and a diode detector. Med Phys 30(8): 1976–1981.

Araki F, Moribe N, Shimonobou T & Yamashita Y (2004) Dosimetric properties of radiophotoluminescent glass rod detector in high-energy photon beams from a linear accelerator and Cyber-Knife. Med Phys 31(7): 1980–1986.

ATGC & Asahi Techno Glass Corporation (2004) Glass dosimetry system, FGD-1000. Instruction Manual Ver.1.3.0.0 or later.

Attix FH (2004) Introduction to Radiological Physics and Radiation Dosimetry. Weinheim, Wiley-VCH.

Benmakhlouf H, Bouchard H, Fransson A & Andreo P (2011) Backscatter factors and mass energy-absorption coefficient ratios for diagnostic radiology dosimetry. Phys Med Biol 56(22): 7179.

Benmakhlouf H, Fransson A & Andreo P (2013) Influence of phantom thickness and material on the backscatter factors for diagnostic x-ray beam dosimetry. Phys Med Biol 58(2): 247.

Bhatt BC & Kulkarni MS (2013) Worldwide Status of Personnel Monitoring using Thermoluminescent (TL), Optically Stimulated Luminescent (OSL) and Radiophotoluminescent (RPL) Dosimeters. International Journal of Luminescence and Applications 3(1): 6–10.

Brenner DJ (2008) Effective dose: a flawed concept that could and should be replaced. The Br J Radiol 81(967): 521–523.

Bridcut RR, Murphy E, Workman A, Flynn P & Winder RJ (2007) Patient dose from 3D rotational neurovascular studies. Br J Radiol 80(953): 362–366.

Brisse HJ, Robilliard M, Savignoni A, Pierrat N, Gaboriaud G, De Rycke Y, Neuenschwander S, Aubert B & Rosenwald J (2009) Assessment of Organ Absorbed Doses and Estimation of Effective Doses From Pediatric Anthropomorphic Phantom Measurements for Multi-Detector Row Ct With and Without Automatic Exposure Control. Health Physics (4): 303–314.

Caracappa PF, Chao TC & Xu XG (2009) A study of predicted bone marrow distribution on calculated marrow dose from external radiation exposures using two sets of image data for the same individual. Health Phys 96(6): 661–674.

Chida K, Inaba Y, Morishima Y, Taura M, Ebata A, Yanagawa I, Takeda K & Zuguch M (2011) Comparison of dose at an interventional reference point between the displayed estimated value and measured value. Radiol Phys Technol 4(2): 189–193.

Chida K, Kato M, Kagaya Y, Zuguchi M, Saito H, Ishibashi T, Takahashi S, Yamada S & Takai Y (2010a) Radiation Dose and Radiation Protection for Patients and Physicians During Interventional Procedure. J Radiat Res 51: 97–105.

Chida K, Kato M, Saito H, Ishibashi T, Takahashi S, Kohzuki M & Zuguchi M (2010b) Optimizing patient radiation dose in intervention procedures. Acta Radiol 51(1): 33–39.

Christner JA, Kofler JM & McCollough CH (2010) Estimating Effective Dose for CT Using Dose–Length Product Compared With Using Organ Doses: Consequences of Adopting International Commission on Radiological Protection Publication 103 or Dual-Energy Scanning. AJR Am J Roentgenol 194: 881–889.

Cloud GC & Markus HS (2003) Diagnosis and management of vertebral artery stenosis. QJM 96(1): 27–54.

Cohnen M, Wittsack HJ, Assadi S, Muskalla K, Ringelstein A, Poll LW, Saleh A & Modder U (2006) Radiation Exposure of Patients in Comprehensive Computed Tomography of the Head in Acute Stroke. AJNR Am J Neuroradiol 27(8): 1741–1745.

Cristy M (1981) Active bone marrow distribution as a function of age in humans. Phys Med Biol 26(3): 389–400.

Cristy M & Eckerman KF (1987) Specific absorbed fractions of energy at various ages from internal photon sources. I. Methods. ORNL, Oak Ridge National Laboratory. TM-8381/V1.

Curry TS, Dowdey JE & Murry RE (1990) Christensen's Physics of Diagnostic Radiology. Philadelphia, Lippincott Williams & Wilkins.

Dauer LT, Thornton RH, Miller DL, Damilakis J, Dixon RG, Marx MV, Schueler BA, Vañó E, Venkatesan A, Bartal G, Tsetis D & Cardella JF (2012) Radiation management for interventions using fluoroscopic or computed tomographic guidance during pregnancy: A joint guideline of the Society of Interventional Radiology and the Cardiovascular and Interventional Radiological Society of Europe with endorsement by the Canadian Interventional Radiology Association. J Vasc Intervent Radiol 23(1): 19–32.

Deak PD, Smal Y & Kalender WA (2010) Multisection CT protocols: sex- and age-specific conversion factors used to determine effective dose from dose-length product. Radiology 257(1): 158–166.

Dendy PP & Heaton B (eds) (1999) Physics for diagnostic radiology. New York, Taylor Francis Group.

Dmitryuk AV, Paramzina SE, Perminov AS, Solov'eva ND & Timofeev NT (1996) The influence of glass composition on the properties of silver-doped radiophotoluminescent phosphate glasses. J Non Cryst Solids 202(1–2): 173–177.

Dowsett DJ, Kenny PA & Johnston RE (2006) The Physics of Diagnostic Imaging. London, Hodder Arnold.

Fan S, Yu C, He D & Hu L (2013) Preparation and Property of Radio-Photoluminescence Dosimeter Glass. Atomic Energy Science and Technology 47(3): 502–507.

Fujiwara H, Momoshima S, Akiyama T & Kuribayashi S (2013) Whole-brain CT digital subtraction angiography of cerebral dural arteriovenous fistula using 320-detector row CT. Neuroradiology (55): 837–843.

Hansch E, Chitkara U, McAlpine J, El-Sayed Y, Dake MD & Razavi MK (1999) Pelvic arterial embolization for control of obstetric hemorrhage: A five-year experience. Am J Obstet Gynecol 180(6): 1454–60.

Hayakawa M, Moritake T, Kataoka F, Takigawa T, Koguchi Y, Miyamoto Y, Akahane K & Matsumaru Y (2010) Direct measurement of patient's entrance skin dose during neurointerventional procedure to avoid further radiation-induced skin injuries. Clin Neurol Neurosurg 112(6): 530–536.

Hendee WR & Ritenour ER (2002) Medical Imaging Physics. New York, Wiley-Liss.

Holmberg O, Czarwinski R & Mettler F (2010a) The importance and unique aspects of radiation protection in medicine. Eur J Radiol 76(1): 6–10.

Holmberg O, Malone J, Rehani M, McLean D & Czarwinski R (2010b) Current issues and actions in radiation protection of patients. Eur J Radiol 76(1): 15–19.

Hough M, Johnson P, Rajon D, Jokisch D, Lee C & Bolch W (2011) An image-based skeletal dosimetry model for the ICRP reference adult male-internal electron sources. Phys Med Biol 56(8): 2309–2346.

Hsu SM, Yang HW, Huang YH, Lee JH, Yu CY, Liao YJ, Hung SK & Lee MS (2010a) Chemical and physical characteristics of self-fabricated radiophotoluminescent glass dosimeter. Radiat Measur 45(3–6): 553–555.

Hsu SM, Yang HW, Yeh TC, Hsu WL, Wu CH, Lu CC, Chen WL & Huang DYC (2007) Synthesis and physical characteristics of radiophotoluminescent glass dosimeters. Radiat Measur 42(4–5): 621–624.

Hsu SM, Yeh SH, Lin MS & Chen WL (2006) Comparison on characteristics of radiophotoluminescent glass dosemeters and thermoluminescent dosemeters. Radiat Prot Dosimetry 119(1–4): 327–331.

Hsu SM, Yung SW, Brow RK, Hsu WL, Lu CC, Wu FB & Ching SH (2010b) Effect of silver concentration on the silver-activated phosphate glass. Mater Chem Phys 123(1): 172–176.

Huang DYC & Hsu SM (2011) Radio-Photoluminescence Glass Dosimeter (RPLGD). Gali-Muhtasib, H (Ed.) Advances in Cancer Therapy,568, InTech.

Hubbell JH (1999) Review of photon interaction cross section data in the medical and biological context. Phys Med Biol 44(1): R1–R22.

Hubbell JH & Seltzer SM (1996) Tables of X-Ray Mass Attenuation Coefficients and Mass Energy-Absorption Coefficients from 1 keV to 20 MeV for Elements Z = 1 to 92 and 48 Additional Substances of Dosimetric Interest. NIST Standard Reference Database 126 NISTIR 5632.

Huda W, Ogden KM & Khorasani MR (2008) Converting dose-length product to effective dose at CT. Radiology 248(3): 995–1003.

IAEA (2007) International Atomic Energy Agency. Dosimetry in Diagnostic Radiology: An International Code of Practice, IAEA TRS 457.

ICRP (1990) International Commission on Radiological Protection, Recommendations of the ICRP. Annals of the ICRP Publication 60, 21(1–3).

ICRP (2007) International Commission on Radiological Protection Recommendations of the ICRP. Annals of the ICRP Publication 103, 37(2–4).

ICRP (2010) International Commission on Radiologic Protection, Radiological Protection in Fluoroscopically Guided Procedures Performed Outside the Imaging Department. Annals of the ICRP Publication 117, 40(6).

ICRP (2012) International Commission on Radiological Protection, ICRP Statement on Tissue Reactions. Early and Late Effects of Radiation in Normal Tissues and Organs. Threshold Doses for Tissue Reactions in a Radiation Protection Context. Annals of the ICRP Publication 118, 41(1/2).

Ihara Y, Kishi A, Kada W, Sato F, Kato Y, Yamamoto T & Iida T (2008) A compact system for measurement of radiophotoluminescence of phosphate glass dosimeter. Radiat Measur 43(2–6): 542–545.

Jones DG (1997) A Realistic Anthropomorphic Phantom for Calculating Organ Doses Arising from External Photon Irradiation. Radiat Prot Dosim 72(1): 21–29.

Jursinic PA (2007) Characterization of optically stimulated luminescent dosimeters, OSLDs, for clinical dosimetric measurements. Med Phys 34(12): 4594–4604.

Kadoya N, Shimomura K, Kitou S, Shiota Y, Fujita Y, Dobashi S, Takeda K, Jingu K, Matsushita H, Namito Y, Ban S, Koyama S & Tabushi K (2012) Dosimetric properties of radiophotoluminescent glass detector in low-energy photon beams. Med Phys 39(10): 5910–5916.

Kalender WA (2011) Computed Tomography: Fundamentals, SystemTechnology, Image Quality, Applications. Germany, John Wiley & Sons.

Kato M, Chida K, Moritake T, Koguchi Y, Sato T, Oosaka H, Tosa T & Kadowaki K (2013) Fundamental study on the characteristics of a radiophotoluminescence glass dosemeter with no energy compensation filter for measuring patient entrance doses in cardiac interventional procedures. Radiat Prot Dosim: pp. 1–6.

Kawaura C, Aoyama T, Koyama S, Achiwa M & Mori M (2006) Organ and effective dose evaluation in diagnostic radiology based on in-phantom dose measurements with novel photodiode-dosemeters. Radiat Prot Dosim 118(4): 421–430.

Klingebiel R, Kentenich M, Bauknecht HC, Masuhr F, Siebert E, Busch M & Bohner G (2008) Comparative evaluation of 64-slice CT angiography and digital subtraction angiography in assessing the cervicocranial vasculature. Vasc Health Risk Manag 4(4): 901–907.

Knežević Ž, Beck N, Milković Đ, Miljanić S & Ranogajec-Komor M (2011) Characterisation of RPL and TL dosimetry systems and comparison in medical dosimetry applications. Radiat Measur 46: 1582–1585.

Knežević Ž, Stolarczyk L, Bessieres I, Bordy JM, Miljanić S & Olko P (2013) Photon dosimetry methods outside the target volume in radiation therapy: Optically stimulated luminescence (OSL), thermoluminescence (TL) and radiophotoluminescence (RPL) dosimetry. Radiat Measur 57(0): 9–18.

Kurobori T, Miyamoto Y, Maruyama Y, Yamamoto T & Sasaki T (2014) A comparative study of optical and radiative characteristics of X-ray-induced luminescent defects in Ag-doped glass and LiF thin films and their applications in 2-D imaging. Nuclear Inst. and Methods in Physics Research, B 326: 76–80.

Lee JH, Lin MS, Hsu SM, Chen IJ, Chen WL & Wang CF (2009) Dosimertry characteristics and performance comparisons: Environmental radiophotoluminescent glass dosemeters versus thermoluminescent dosemeters. Radiat Measur 44(1): 86–91.

Lell MM, Ditt H, Panknin C, Sayre JW, Ruehm SG, Klotz E, Tomandl BF & Villablanca JP (2007) Bone-Subtraction CT Angiography: Evaluation of Two Different Fully Automated Image-Registration Procedures for Interscan Motion Compensation. AJNR Am J Neuroradiol 28(7): 1362–1368.

Ludlow JB, Davies-Ludlow LE, Brooks SL & Howerton WB (2006) Dosimetry of 3 CBCT devices for oral and maxillofacial radiology: CB Mercuray, NewTom 3G and i-CAT. Dentomaxillofac Radiol 35(4): 219–226.

Ma CM & Seuntjens JP (1999) Mass-energy absorption coefficient and backscatter factor ratios for kilovoltage x-ray beams. Phys Med Biol 44(1): 131.

Mamourian AC, Pukenas BA & Satti SR (2013) Should American Journal of Neuroradiology Commentary Be Evidence-Based? AJNR Am J Neuroradiol 34(8): E97–E98.

Martin CJ (2007) Effective dose: how should it be applied to medical exposure? Br J Radiol 80(956): 639–647.

Matsubara K, Koshida K, Suzuki M, Shimono T, Yamamoto T & Matsui O (2009) Effective dose evaluation of multidetector CT examinations: influence of the ICRP recommendation in 2007. Eur Radiol 19: 2855–2861.

Matsubara K, Koshida K, Noto K & Takata T (2011) Reduction of breast dose in abdominal CT examinations: Effectiveness of automatic exposure control system. Radiat Measur 46(12): 2056–2059.

McCollough CH, Christner JA & Kofler JM (2010) How Effective Is Effective Dose as a Predictor of Radiation Risk? AJR Am J Roentgenol 194: 890–896.

McCollough CH, Leng S, Yu L, Cody DD, Boone JM & McNitt-Gray MF (2011) CT Dose Index and Patient Dose: They Are Not the Same Thing. Radiology 259(2): 311–316.

McCollough CH, Primak AN, Braun N, Kofler J, Yu L & Christner J (2009) Strategies for Reducing Radiation Dose in CT. Radiol Clin North Am 47(1): 27–40.

McCollough CH, Schueler BA, Atwell TD, Braun NN, Regner DM, Brown DL & LeRoy AJ (2007) Radiation Exposure and Pregnancy: When Should We Be Concerned? RadioGraphics (27): 909–918.

McKinney AM, Palmer CS, Truwit CL, Karagulle A & Teksam M (2008) Detection of Aneurysms by 64-Section Multidetector CT Angiography in Patients Acutely Suspected of Having an Intracranial Aneurysm and Comparison with Digital Subtraction and 3D Rotational Angiography. AJNR Am J Neuroradiol 29(3): 594–602.

Miller DL, Balter S, Schueler BA, Wagner LK, Strauss KJ & Vañó E (2010) Clinical radiation management for fluoroscopically guided interventional procedures. Radiology 257(2): 321–332.

Miyamoto Y, Takei Y, Nanto H, Kurobori T, Konnai A, Yanagida T, Yoshikawa A, Shimotsuma Y, Sakakura M, Miura K, Hirao K, Nagashima Y & Yamamoto T (2011) Radiophotoluminescence from silver-doped phosphate glass. Radiat Measur 46(12): 1480–1483.

Miyamoto Y, Yamamoto T, Kinoshita K, Koyama S, Takei Y, Nanto H, Shimotsuma Y, Sakakura M, Miura K & Hirao K (2010) Emission mechanism of radiophotoluminescence in Ag-doped phosphate glass. Radiat Measur 45(3–6): 546–549.

Mizuno H, Kanai T, Kusano Y, Ko S, Ono M, Fukumura A, Abe K, Nishizawa K, Shimbo M, Sakata S, Ishikura S & Ikeda H (2008) Feasibility study of glass dosimeter postal dosimetry audit of high-energy radiotherapy photon beams. Radiother Oncol, 86(2): 258–263.

Mooney RB & McKinstry J (2001) Paediatric dose reduction with the introduction of digital fluorography. Radiat Prot Dosim 94(1–2): 117–120.

Moritake T, Matsumaru Y, Takigawa T, Nishizawa K, Matsumura A & Tsuboi K (2008) Dose Measurement on Both Patients and Operators during Neurointerventional Procedures Using Photoluminescence Glass Dosimeters. AJNR Am J Neuroradiol 29(10): 1910–1917.

Moritake T, Hayakawa M, Matsumaru Y, Takigawa T, Koguchi Y, Miyamoto Y, Mizuno Y, Chida K, Akahane K, Tsuboi K, Sakae T & Sakurai H (2011) Precise mapping system of entrance skin dose during endovascular embolization for cerebral aneurysm. Radiat Measur 46(12): 2103–2106.

Moscovitch M & Horowitz YS (2007) Thermoluminescent materials for medical applications: LiF:Mg,Ti and LiF:Mg,Cu,P. Radiat Measur 41(Supplement 1): S71–S77.

Nakagawa K, Koyanagi H, Shiraki T, Saegusa S, Sasaki K, Oritate T, Mima K, Miyazawa M, Ishidoya T, Ohtomo K & Yoda K (2005) A radiophotoluminescent glass plate system for medium-sized field dosimetry. Rev Sci Instrum 76(10): 106–104.

Nikolic B, Spies JB, Campbell L, Walsh SM, Abbara S & Lundsten MJ (2001) Uterine Artery Embolization: Reduced Radiation with Refined Techniqueith. Journal of Vascular and Interventional Radiology 12(1): 39–44.

Nikolic B, Spies JB, Lundsten MJ & Abbara S (2000) Patient Radiation Dose Associated with Uterine Artery Embolization. Radiology 214(1): 121–125.

Nishizawa K, Masuda Y, Morinaga K, Suzuki S, Kikuyama S, Yoshida T, Ohno M, Akahane K & Iwai K (2008) Surface dose measurement in patients and physicians and effective dose estimation in patients during uterine artery embolisation. Radiat Prot Dosim 128(3): 343–350.

Nishizawa K, Moritake T, Matsumaru Y, Tsuboi K & Iwai K (2003) Dose measurement for patients and physicians using a glass dosemeter during endovascular treatment for brain disease. Radiat Prot Dosim 107(4): 247–252.

Oberhofer M & Scharmann A (eds) (1993) Techniques and Management of Personnel Thermoluminescence Dosimetry Services, Health Physics and Radiation Protection, Volume 2. The Netherlands, Kluwer Academic Publishers.

Ohki T & Veith FJ (2000) Endovascular Grafts and Other Image-Guided Catheter-Based Adjuncts to Improve the Treatment of Ruptured Aortoiliac Aneurysms. Ann Surg 232(4): 466–479.

Ojala K, Perälä J, Kariniemi J, Ranta P, Raudaskoski T & Tekay A (2005) Arterial embolization and prophylactic catheterization for the treatment for severe obstetric hemorrhage. Acta Obstet Gynecol Scand 84(11): 1075–1080.

Perry JA (1987) RPL dosimeter, Radiophotoluminescence in Health Physics. Bristol, Adam Hilger.

Petoussi-Henss N, Zankl M, Drexler G, Panzer W & Regulla D (1998) Calculation of backscatter factors for diagnostic radiology using Monte Carlo methods. Phys Med Biol 43(8): 2237–2250.

Piesch E & Burgkhardt B (1994) Photoluminescence dosimetry : the alternative in personnel monitoring. Radioprotection 29(1): 39–67.

Piesch E, Burgkhardt B & Vilgis (INVITED) M (1990) Photoluminescence Dosimetry: Progress and Present State of Art. Radiat Prot Dosim 33(1–4): 215–226.

Piesch E, Burgkhardt B & Vilgis M (1993) Progress in Phosphate Glass Dosimetry: Experiences and Routine Monitoring with a Modern Dosimetry System. Radiat Prot Dosim 47(1–4): 409–414.

Psychogios MN, Schramm P, Amelung N, Pilgram-Pastor SM, Gröschel K, Wasser K, Frölich AM, Mohr A & Knauth M (2013) Evaluation of Noninvasive Follow-up Methods for the Detection of Intracranial In-Stent Restenosis: A Phantom Study. Invest Radiol 48(2): 98–103.

Ragozzino MW, Gray JE, Burke TM & Van Lysel MS (1981) Estimation and minimization of fetal absorbed dose: data from common radiographic examinations. AJR Am J Roentgenol 137(4): 667–671.

Rah JE, Hong JY, Kim GY, Kim YL, Shin DO & Suh TS (2009a) A comparison of the dosimetric characteristics of a glass rod dosimeter and a thermoluminescent dosimeter for mailed dosimeter. Radiat Measur 44(1): 18–22.

Rah JE, Kim S, Cheong KH, Lee JW, Chung JB, Shin DO & Suh TS (2009b) Feasibility study of radiophotoluminescent glass rod dosimeter postal dose intercomparison for high energy photon beam. Appl Radiat Isot 67(2): 324–328.

Rah JE, Hwang UJ, Jeong H, Lee SY, Lee DH, Shin DH, Yoon M, Lee SB, Lee R & Park SY (2011) Clinical application of glass dosimeter for in vivo dose measurements of total body irradiation treatment technique. Radiat Measur 46(1): 40–45.

Riesen H & Liu Z (eds) (2012) Optical Storage Phosphors and Materials for Ionizing Radiation, Current Topics in Ionizing Radiation Research. Mitsuru, N. (Ed.), InTech.

Romijn M, van Andel HAFG, van Walderveen MA, Sprengers ME, van Rijn JC, van Rooij WJ, Venema HW, Grimbergen CA, den Heeten GJ & Majoie CB (2008) Diagnostic Accuracy of CT Angiography with Matched Mask Bone Elimination for Detection of Intracranial Aneurysms: Comparison with Digital Subtraction Angiography and 3D Rotational Angiography. AJNR Am J Neuroradiol 29(1): 134–139.

Sakamoto S, Kiura Y, Shibukawa M, Ohba S, Arita K & Kurisu K (2006) Subtracted 3D CT Angiography for Evaluation of Internal Carotid Artery Aneurysms: Comparison with Conventional Digital Subtraction Angiography. AJNR Am J Neuroradiol 27(6): 1332–1337.

Scalzetti EM, Huda W, Bhatt S & Ogden KM (2008) A Method To Obtain Mean Organ Doses in A Rando Phantom. Health Physics 95(2): 242–244.

Seuntjens J, Thierens H, Van der Plaetsen A & Segaert O (1987) Conversion factor f for X-ray beam qualities, specified by peak tube potential and HVL value. Phys Med Biol 32(5): 595–603.

Shivaramu (2002) Effective atomic numbers for photon energy absorption and photon attenuation of tissues from human organs. Medical Dosimetry 27(1): 1–9.

Sommer M & Henniger J (2006) Investigation of a BeO-based optically stimulated luminescence dosemeter. Radiat Prot Dosim 119(1–4): 394–397.

Strauss KJ (2006) Pediatric interventional radiography equipment: safety considerations. Pediatr Radiol 36 (Suppl 2): 126–135.

Struffert T, Hauer M, Banckwitz R, Köhler C, Royalty K & Doerfler A (2014) Effective dose to patient measurements in flat-detector and multislice computed tomography: a comparison of applications in neuroradiology. Eur Radiol (24): 1257–1265.

STUK (2013) Radiologisten tutkimusten ja toimenpiteiden määrät vuonna 2011. STUK Radiation and Nuclear Safety Authority, Finland STUK-B 161.

Sun L, Mizuno Y, Iwamoto M, Goto T, Koguchi Y, Miyamoto Y, Tsuboi K, Chida K & Moritake T (2014) Direct measurement of a patient's entrance skin dose during pediatric cardiac catheterization. J Radiat Res: 1–9.

Takayuki N, Masahiko K, Ken Y, Kinji N, Junichi S, Takeshi O & Didier P (2005) In vivo dosimetry of high-dose-rate brachytherapy: Study on 61 head-and-neck cancer patients using radiophotoluminescence glass dosimeter. Int J Radiat Oncol Biol Phys 61(3): 945–953.

Takayuki N, Masahiko K, Ken Y, Kinji N, Junichi S, Takeshi O, Takuyo K, Kotaro G, Masahiko O & Iori S (2008) In Vivo Dosimetry of High-Dose-Rate Interstitial Brachytherapy in the Pelvic Region: Use of a Radiophotoluminescence Glass Dosimeter for Measurement of 1004 Points in 66 Patients With Pelvic Malignancy. Int J Radiat Oncol Biol Phys 70(2): 626–633.

Tapiovaara M & Siiskonen T (2008) PCXMC – a Monte Carlo Program for Calculating Patient Doses in Medical X-Ray Examinations, STUK – Radiation and Nuclear Safety Authority, Finland STUK-A 231: 3–49.

Tapiovaara M & Tapiovaara T (2008) The validation and user's manual of the Spektripaja (2.0) program (In Finnish). STUK-TR 3 2.0: 33.

Teksam M, McKinney A, Cakir B & Truwit CL (2005) Multi-slice CT angiography of small cerebral aneurysms: is the direction of aneurysm important in diagnosis? Eur J Radiol 53(3): 454–462.

Teksam M, McKinney A, Casey S, Asis M, Kieffer S & Truwit CL (2004) Multi-Section CT Angiography for Detection of Cerebral Aneurysms. AJNR Am J Neuroradiol 25(9): 1485–1492.

Toivonen M & Komppa T (2003) Report on methods of evaluating local skin dose in interventional radiology. Report of the DIMOND III working group of Work Package 3.1. STUK – Radiation and Nuclear Safety Authority, Finland.

Tomandl BF, Hammen T, Klotz E, Ditt H, Stemper B & Lell M (2006) Bone-Subtraction CT Angiography for the Evaluation of Intracranial Aneurysms. AJNR Am J Neuroradiol 27(1): 55–59.

Uchiyama D, Koganemaru M, Abe T, Hori D & Hayabuchi N (2008) Arterial catheterization and embolization for management of emergent or anticipated massive obstetrical hemorrhage. Radiat Med (26): 188–197.

UNSCEAR (2008) United Nations Scientific Committee on the Effects of Atomic Radiation. Sources and Effects of Ionizing Radiation, Report to the General Assembly Scientific Annexes A: Medical radiation exposures. UNSCEAR Volume I.

UNSCEAR (2013) United Nations Scientific Committee on the Effects of Atomic Radiation. Sources and Effects of Ionizing Radiation, Report to the General Assembly Scientific Annexes B: Effects of radiation exposure of children. UNSCEAR VolumeII.

Wall BF, Kendall GM, Edwards AA, Bouffler S, Muirhead CR & Meara JR (2006) What are the risks from medical X-rays and other low dose radiation? Br J Radiol 79(940): 285–294.

Watanabe Y, Uotani K, Nakazawa T, Higashi M, Yamada N, Hori Y, Kanzaki S, Fukuda T & Naito N (2009) Dual-energy direct bone removal CT angiography for evaluation of intracranial aneurysm or stenosis: comparison with conventional digital subtraction angiography. Eur Radiol 19: 1019–1024.

Watanabe Y, Kashiwagi N, Yamada N, Higashi M, Fukuda T, Morikawa S, Onishi Y, Iihara K, Miyamoto S & Naito H (2008) Subtraction 3D CT Angiography with the Orbital Synchronized Helical Scan Technique for the Evaluation of Postoperative Cerebral Aneurysms Treated with Cobalt-Alloy Clips. AJNR Am J Neuroradiol 29(6): 1071–1075.

Wortman A, Miller DL, Donahue TF & Petersen S (2013) Embolization of renal hemorrhage in pregnancy. Obstet Gynecol 121(2 PART 2): 480–483.

Wrixon AD (2008) New recommendations from the International Commission on Radiological Protection—a review. Phys Med Biol 53(8): 41–60.

Yamamoto T, Maki D, Sato F, Miyamoto Y, Nanto H & Iida T (2011) The recent investigations of radiophotoluminescence and its application. Radiat Measur 46(12): 1554–1559.

Yokota R, Muto Y, Naoi J & Yamaji I (1971) Silver-activated phosphate dosimeter glasses with low energy dependence and higher sensitivity. Health physics 20: 662.

Zhang LJ, Wu SY, Niu JB, Zhang ZL, Zhang Z.L., Zhao, Y.E., Chai X, Zhou CS & Lu GM (2010) Dual-Energy CT Angiography in the Evaluation of Intracranial Aneurysms: Image Quality, Radiation Dose, and Comparison With 3D Rotational Digital Subtraction Angiography AJR Am J Roentgenol 194: 23–30.

Zoetelief J, Julius HW & Christensen P (2000) Recommendations for Patient Dosimetry in Diagnostic Radiology Using TLD. Office for Official Pubplications of the European Communities, EUR 19604.

Original publications

I Manninen AL; Koivula A; Nieminen MT (2012) The applicability of radiophotoluminescence dosemeter (RPLD) for measuring medical radiation (MR) doses. Radiat Prot Dosim 151(1): 1–9.

II Manninen AL; Ojala P; Nieminen MT; Perälä J (2014) Fetal Radiation Dose in Prophylactic Uterine Arterial Embolization. CardioVascular Intervent Radiol, 37(4): 942–948.

III Manninen AL; Isokangas JM; Karttunen A; Siniluoto T; Nieminen MT (2012) A Comparison of Radiation Exposure between Diagnostic CTA and DSA Examinations of Cerebral and Cervicocerebral Vessels. Am J Neuroradiol 33(11): 2038–2042.

Original publications are not included in the electronic version of the dissertation.

Book orders:
Granum: Virtual book store
http://granum.uta.fi/granum/

UNIVERSITY OF OULU P.O. Box 8000 FI-90014 UNIVERSITY OF OULU FINLAND

ACTA UNIVERSITATIS OULUENSIS

ISBN 978-952-62-0623-3 (Paperback)
ISBN 978-952-62-0624-0 (PDF)
ISSN 0355-3221 (Print)
ISSN 1796-2234 (Online)

UNIVERSITY of OULU
OULUN YLIOPISTO